Journal of
MATERIALS RESEARCH

Thin films for superconducting electronics: Precursor performance issues, deposition mechanisms, and superconducting phase formation-processing strategies in the growth of $Tl_2Ba_2CaCu_2O_8$ films by metal-organic chemical vapor deposition

Bruce J. Hinds, Richard J. McNeely, Daniel B. Studebaker, and Tobin J. Marks
Department of Chemistry and the Science and Technology Center for Superconductivity, Northwestern University, Evanston, Illinois 60208-3113

Timothy P. Hogan, Jon L. Schindler, and Carl R. Kannewurf
Department of Electrical Engineering and Computer Science and the Science and Technology Center for Superconductivity, Northwestern University, Evanston, Illinois 60208-3113

Xiao Feng Zhang and Dean J. Miller
Materials Science Division and the Science and Technology Center for Superconductivity, Argonne National Laboratory, Argonne, Illinois 60439

(Received 22 February 1996; accepted 17 December 1996)

Epitaxial $Tl_2Ba_2CaCu_2O_8$ thin films with excellent electrical transport characteristics are grown in a two-step process involving metal-organic chemical vapor deposition (MOCVD) of a BaCaCuO(F) thin film followed by a postanneal in the presence of Tl_2O vapor. Vapor pressure characteristics of the recently developed liquid metal-organic precursors $Ba(hfa)_2 \cdot mep$ (hfa = hexafluoroacetylacetonate, mep = methylethylpentaglyme), $Ca(hfa)_2 \cdot tet$ (tet = tetraglyme), and the solid precursor $Cu(dpm)_2$ (dpm = dipivaloylmethanate) are characterized by low pressure thermogravimetric analysis. Under typical film growth conditions, transport is shown to be diffusion limited. The transport rate of $Ba(hfa)_2 \cdot mep$ is demonstrated to be stable for over 85 h at typical MOCVD temperatures (120 °C). In contrast, the vapor pressure stability of the commonly used Ba precursor, $Ba(dpm)_2$, deteriorates rapidly at typical growth temperatures, and the decrease in vapor pressure is approximately exponential with a half-life of ~9.4 h. These precursors are employed in a low pressure (5 Torr) horizontal, hot-wall, film growth reactor for growth of BaCaCuO(F) thin films on (110) $LaAlO_3$ substrates. From the dependence of film deposition rate on substrate temperature and precursor partial pressure, the kinetics of deposition are shown to be mass-transport limited over the temperature range 350–650 °C at a 20 nm/min deposition rate. A ligand exchange process which yields volatile $Cu(hfa)_2$ and Cu(hfa)(dpm) is also observed under film growth conditions. The MOCVD-derived BaCaCuO(F) films are postannealed in the presence of bulk $Tl_2Ba_2CaCu_2O_8$ at temperatures of 720–890 °C in flowing atmospheres ranging from 0–100% O_2. The resulting $Tl_2Ba_2CaCu_2O_8$ films are shown to be epitaxial by x-ray diffraction and transmission electron microscopic (TEM) analysis with the *c*-axis normal to the substrate surface, with in-plane alignment, and with abrupt film-substrate interfaces. The best films exhibit a T_c = 105 K, transport-measured $J_c = 1.2 \times 10^5$ A/cm^2 at 77 K, and surface resistances as low as 0.4 mΩ (40 K, 10 GHz).

I. INTRODUCTION

With the discovery of high temperature superconducting (HTS) materials, there has been great interest in applications to thin film electronic devices such as Josephson junctions for magnetic field detection[1–3] or ultrafast computation,[4,5] for interconnects in multichip modules,[6,7] and in bolometric detectors.[8,9] Also of interest are applications in passive microwave devices such as delay lines and filters that utilize the inherently low surface resistance of HTS materials.[10–14] This latter technology is likely to be a large-scale application of HTS thin films and would significantly impact cellular telecommunication.[15] Numerous laboratory examples of

such microwave devices have been demonstrated for $YBa_2Cu_3O_{7-x}$ films.[16–21] The $Tl_mBa_2Ca_{n1}Cu_nO_{2(n+1)+m}$ (TBCCO) superconductors[22] have also attracted interest for use in microwave devices due to the high critical temperatures (up to 125 K). To date, the lowest HTS film surface resistances (R_s values as low as 0.024 mΩ at 5 K, 10 GHz) have been reported for $Tl_2Ba_2Ca_2Cu_3O_{10}$ (Tl-2223) films.[23] $Tl_2Ba_2CaCu_2O_8$ (Tl-2212) films (T_c = 108 K, surface resistances as low as 0.025 mΩ at 5 K, 10 GHz) are also of interest because of the greater phase stability versus Tl-2223,[24] Thin Tl-2212 films with very low R_s values have been grown by laser ablation,[25–27] sputtering,[24,28–31] and metal-organic chemical vapor deposition (MOCVD).[32,33] Several TBCCO delay line and resonator devices using films derived from physical vapor deposition (PVD) growth processes have been demonstrated.[30,34–36]

With regard to large-scale HTS film growth, MOCVD processes offer the attraction of simplicity of apparatus, independence from line-of-site deposition, ability to coat large areas and complex shapes, benefits of high throughput, and possibility of film growth under highly oxidizing conditions. The application of MOCVD to HTS materials has been recently reviewed.[37–40] Though several reports on the growth of Tl-2212,[41–44] Tl-2223,[45,46] and Tl-1223[47,48] films by MOCVD have appeared, metal-organic precursor characteristics, film growth mechanisms, phase formation processes, and the device suitability of the resulting Tl-2212 films have yet to be investigated in depth. Although there is one report of bandpass filter fabrication using MOCVD-derived Tl-2212 films on metallic substrates, performance is not detailed, and R_s is relatively high (18 mΩ at 35 GHz, 88 K).[32] Hence, there is a need to characterize TBCCO MOCVD processes in detail and to investigate the microstructural and transport properties of the resulting films.

MOCVD processes are by nature complex, and a number of important issues must be addressed regarding applications to HTS materials.[49,50] Crucial is the development of suitably volatile metal-organic precursors. Particularly problematic are electropositive metals with large ionic radii and coordination numbers, such as Ba^{2+} and Sr^{2+}, which are difficult to coordinatively saturate without forming involatile oligomers. The commonly used Ba MOCVD precursor, "$Ba(dpm)_2$" (dpm = dipivaloylmethanate), relies on the steric encumbrance of the dpm ligand to impede oligomerization typical of high Ba^{2+} coordination numbers (9–10). This approach is marginally effective,[59] resulting in the formation of poorly volatile oligomers at temperatures approaching the decomposition temperature (240 °C), and suffers from poor vapor pressure stability.[51–59] Without a stable metal source pressure, MOCVD film growth processes become uncontrollable. Another synthetic approach is to saturate the metal coordination sphere with an ancillary, neutrally charged Lewis base (e.g., a polyether). However, this requires the use of electron-withdrawing β-diketonate ligands (e.g., hfa = hexafluoroacetylacetonate) to generate sufficient metal acidity.[45,60] Thus, $Ba(hfa)_2 \cdot tet$ (tet = tetraglyme) has been shown to exhibit substantially increased vapor pressure[61] over $Ba(dpm)_2$, and utility has been demonstrated in MOCVD growth of HTS materials.[45] With regard to precursor characterization, equilibrium vapor pressure is difficult to measure accurately, and there is a need to develop methods that can efficiently and accurately characterize precursor volatility in terms of nonequilibrium vapor pressure, diffusion coefficient, and long-term stability under film growth conditions. In addition to precursor development and characterization, there is a need to understand the chemisorption/decomposition mechanisms involved in forming crystalline oxide thin films. Growth kinetics have been approximately determined for $YBa_2Cu_3O_{7-x}$ deposition using dpm-based precursors.[50,62,63] However, to date little is known about the kinetics or film growth mechanisms for fluorinated MOCVD precursors under reaction conditions used for HTS film growth.

A further challenge in TBCCO film growth lies in understanding the inherently complex phase relationships of the TBCCO superconductor family which arise from the volatility of Tl_2O. In a convenient open flow thallination process as implemented here, variables such as O_2 pressure, growth temperatures, and heating rates can be explored. The challenge is to develop a reliable synthetic scheme for forming phase-pure Tl-2212 films with optimized transport and R_s properties.

Discussed here is a detailed account of an MOCVD process for the growth of high-quality Tl-2212 thin films. Volatile MOCVD precursors, including the recently developed liquid precursor $Ba(hfa)_2 \cdot mep$ (mep = methylethylpentaglyme),[64] are characterized by an efficient, reduced-pressure TGA (thermogravimetric analysis) technique. This method quickly and reliably characterizes precursors in terms of vapor pressure, diffusion, and thermal stability under MOCVD growth conditions. An efficient MOCVD reactor is described and is used to study the kinetics of BaCaCuO(F) film growth on $LaAlO_3$. In the study of BaCaCuO(F) thin film deposition, by-products are trapped and analyzed by mass spectrometry, revealing competing ligand exchange processes. An effective open flow thallination/annealing scheme for BaCaCuO(F) precursor thin films is implemented for the formation of high-quality, epitaxial Tl-2212 films with excellent transport and microwave R_s properties. These films are characterized by x-ray diffraction, scanning and transmission electron microscopy, profilometry, magnetic hysteresis, dc electrical transport, and microwave surface resistance.

II. EXPERIMENTAL

A. Metal-organic precursors

$Ba(hfa)_2 \cdot mep$,[64] $Ca(hfa)_2 \cdot tet$, and $Cu(dpm)_2$ (hfa = hexafluoroacetylacetoneate, dpm = dipivaloylmethanate, mep = methylethylpentaglyme, tet = tetraglyme) were prepared as described in the literature[65] from high purity (99.999%) metal salts. Purity was confirmed by ^1H NMR analysis and melting point. For comparative sublimation studies, $Ba(dpm)_2$ was synthesized under anhydrous conditions from the reaction of Ba metal with Hdpm in THF solution, with subsequent removal of solvent and excess ligand.[66] $Ba(dpm)_2$ was stored under a N_2 atmosphere in a glove box.

B. TGA characterization

Precursor evaporation rates were measured with a TA Instruments STD 2960 simultaneous thermogravimetric-differential thermal analysis (TGA-DTA) apparatus using the experimental configuration shown in Fig. 1. The TGA-DTA experiment directs a horizontal carrier gas flow across 3.60 mm deep × 3.69 mm diameter alumina sample pans mounted on microbalance arms. Precursor powders were loaded and compressed to fill the sample pans which were then weighed. Approximately 1/3 of the sample weight was then removed and the remainder weighed to provide a defined diffusion distance. The system pressure was adjusted via control of the purified grade N_2 flow rate (50–100 sccm) and by a throttle valve connected to a 14 cfm direct drive Fisher Maxima D16A vacuum pump. Pressure was measured with an MKS 122AA capacitance manometer. Evaporation rates at a given temperature were determined from the derivative of sample weight with respect to time during a temperature ramp of 1.5 °C/min from 80–250 °C.

C. MOCVD film growth

The research MOCVD reactor used in this study (Fig. 2) is of a horizontal design. Metal-organic precursor reservoirs are individually heated by thermostated oil baths, and argon carrier flows are mixed in a common manifold. Precursors are maintained *in vacuo* or under atmospheric pressure of argon while being heated, to prevent reaction with atmospheric moisture. For uniformity of deposition rate over large substrate areas, a quartz laminar flow chamber is utilized. The 3 : 1 aspect ratio of cross section width-to-height (6.0 × 2.0 cm) in this flow chamber reduces thermal buoyancy effects, thus enhancing the stability of the carrier flow.[67] A SiC-coated graphite susceptor is positioned at the end of the flow chamber and is angled at 8.7° to aid uniformity of deposition along the length of the substrate. The susceptor is heated by a 6 kW, water-cooled IR (infrared) lamp (Research Inc.), and temperature is monitored with a *K*-type thermocouple on the surface of the susceptor. Ar and O_2 carrier flows are regulated by Unit 1400A mass flow controllers. H_2O flow is controlled by the O_2 flow and a constant bleed valve setting, with H_2O flow rates determined by weight loss. Pressure is controlled by a throttle valve and is measured by an MKS 122AA capacitance manometer. Typical film growth conditions are listed in Table I. To determine film stoichiometry and deposition rates, the metal content of the 1.0 × 1.0 cm^2 BaCaCuO(F) films is assayed by dissolvation in an aqueous 1.0 M HNO_3 solution. The metal content is then determined using an AtomScan 25 ICP atomic emission spectrometer monitoring the Ba 455.4 nm, Ca 393.3 nm, and Cu 324.7 nm lines at a plasma power of 1150 W. Analysis uses a 2-point calibration curve with standards near 50 μm concentration. The stoichiometries found for different films located at different places over the entire 5.0 × 5.0 cm area of the susceptor are identical to within the precision of the ICP assay (±3%).

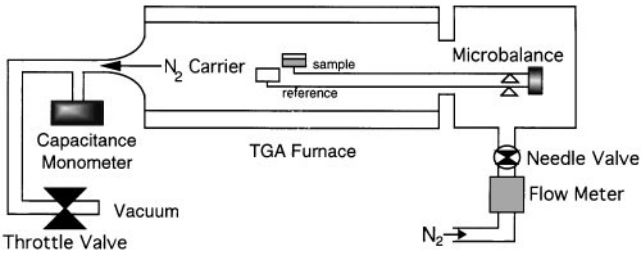

FIG. 1. Schematic diagram of the horizontal, reduced pressure thermogravimetric analysis (TGA) instrumentation utilized in the study of MOCVD precursor volatility.

D. Precursor by-product trapping study

In the by-product trapping study, a 0 °C trap was placed in the reactor bypass line 10 cm downstream from the bypass valve as shown in Fig. 3. A small tube furnace maintained at 400 °C was placed around the bypass line between the bypass valve and the trap to simulate reactor conditions. The same precursor temperatures and gas flows as in Table I were employed with the exception of the oxidizer gas flow. Three trials of varying oxidizer gas flow were performed: one with 100 sccm O_2 + 250 sccm H_2O, one with 350 O_2 sccm and no H_2O, and a control with neither O_2 nor H_2O, but 350 sccm Ar. The solids collected in the trap were analyzed with a VG 70-SE mass spectrometer using the direct injection method. For the MOCVD oxidizer flow 100 sccm O_2 + 250 sccm H_2O, trapped products having the following mass spectral features were identified: [EI^+, 70 eV, m/z^+, $P_{Ba} = Ba(hfa)_2 \cdot mep$, $P_{Ca} = Ca(hfa)_2 \cdot tet$, $P_{Cu} = Cu(dpm)_2$] 625 (P_{Ba} − hfa), 567 [$Ba(hfa)_2 \cdot tet$ − hfa],

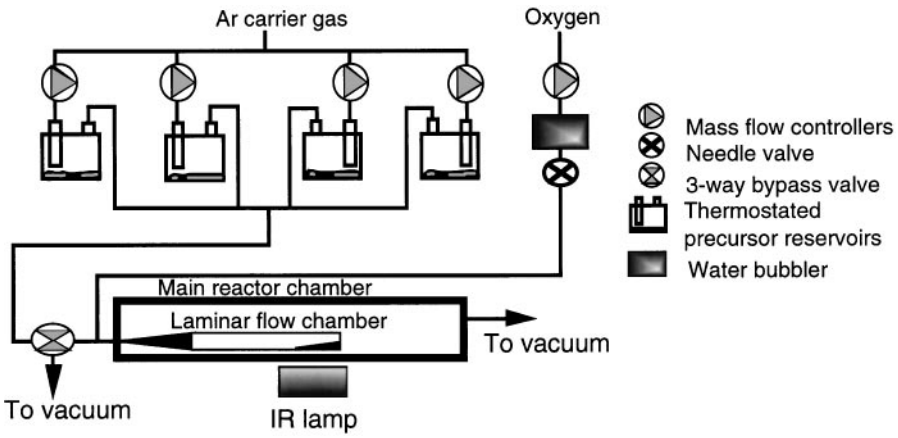

FIG. 2. Schematic diagram of the horizontal hot-wall MOCVD film growth reactor utilized in this study.

527 (P_{Ba} − hfa − CF_3CO), 477 [$Cu(hfa)_2$], 469 (P_{Ca} − hfa), 453 [Cu(dpm)(hfa)], 437 (BaF•mep), 429 (P_{Cu}), 408 [$Cu(hfa)_2$ − CF_3], 396 [Cu(hfa)(dpm) − $C(CH_3)_3$], 339 [Cu(hfa)CF_3], 345 [Ba(hfa)], 246 [Cu(dpm)], 201 [Cu(hfa) − CF_3], 189 [P_{Cu} − dpm − $C(CH_3)_3$], 103 (tet − $C_5H_{11}O_3$). For an oxidizer flow of 350 sccm O_2, the following mass spectral features were observed: 832 (P_{Ba}), 669 (P_{Ba} − $C_7H_{15}O_4$), 625 (P_{Ba} − hfa), 567 [$Ba(hfa)_2$•tet − hfa], 527 (P_{Ba} − hfa − CF_3 CO), 477 [$Cu(hfa)_2$], 453 [Cu(dpm)(hfa)], 437 (BaF•mep), 429 (P_{Cu}), 396 [P_{Cu}(dpm)(hfa) − $C(CH_3)_3$], 372 [P_{Cu} − $C(CH_3)_3$], 345 [Ba(hfa)], 246 [Cu(dpm)], 209 (Hhfa), 189 [Cu(dpm)(hfa) − dpm − $C(CH_3)_3$], 103 (tet − $C_5H_{11}O_3$). As control experiments to examine gas phase ligand exchange, the following transport conditions were utilized and trapped products analyzed. Without oxidizer stream (350 sccm Ar carrier) and without passing through the 400 °C hot zone: 625 (P_{Ba} − hfa), 567 [$Ba(hfa)_2$•tet − hfa], 527 (P_{Ba} −hfa − CF_3-CO), 469 (P_{Ca} − hfa), 429 (P_{Cu}), 372 [P_{Cu} − $C(CH_3)_3$], 345 [Ba(hfa)], 315 [P_{Cu} − $2C(CH_3)_3$], 281 [Ca(hfa)], 246 [Cu(dpm)], 189 [Cu(dpm) − $C(CH_3)_3$], 127 [dpm − $C(CH_3)_3$], 103 (tet − $C_5H_{11}O_3$). With fresh $Ba(hfa)_2$•mep not transported under MOCVD conditions, mass spectral features: 832 (P_{Ba}), 669 (P_{Ba} − $C_7H_{15}O_4$), 625 (P_{Ba} − hfa), 527 (P_{Ba} − hfa − CF_3CO, 437 (BaF•mep), 345 [Ba(hfa)], 209 (Hhfa), 103 (tet − $C_5H_{11}O_3$). For mixed fresh samples of $Ba(hfa)_2$•mep and $Ca(hfa)_2$•tet, not transported under MOCVD conditions, mass spectral features: 625 (P_{Ba} − hfa), 567 [$Ba(hfa)_2$•tet − hfa], 527 (P_{Ba} − hfa − CF_3CO), 523 (P_{Ba} − hfa − C_2H_4O), 469 (P_{Ca} − hfa), 425 (P_{Ca} − hfa − C_2H_4O).

TABLE I. Typical MOCVD conditions for the deposition of BaCaCuO(F) thin films from $Ba(hfa)_2$•mep, $Ca(hfa)_2$•tet, and $Cu(dpm)_2$ precursors in the horizontal MOCVD reactor shown in Fig. 2.

Precursor reservoir temperatures	116° $Ba(hfa)_2$•mep
	90° $Ca(hfa)_2$•tet
	108° $Cu(dpm)_2$
Precursor carrier flow	50 sccm each
O_2/H_2O flow	100/250 sccm
Total pressure	5 Torr
Substrate temperature	500 °C
Growth rate	20 nm/min
Run time	40 min
Substrate	(110) single crystal $LaAlO_3$

E. $Tl_2Ba_2Ca_{n-1}Cu_nO_{4+2n}$ phase formation

Due to the high volatility and extreme reactivity of Tl_2O, it is difficult to grow TBCCO films using an *in situ* process (i.e., one not requiring a postanneal). The present MOCVD-derived precursor BaCaCuO(F) films were thus reacted with an equilibrium pressure of Tl_2O vapor originating from a bulk TBCCO pellet maintained at a constant temperature between 720 and 900 °C. The 1.0 g pressed pellet (1.0 cm diameter × 3.0 mm thick) was prepared from presintered Tl_2O_3, BaO, CaO, CuO powders (Aldrich) with Tl : Ba : Ca : Cu stoichiometry ratios of 2 : 2 : 1 : 2. The film was supported face down over the pellet with a gold foil mount and crimp-sealed

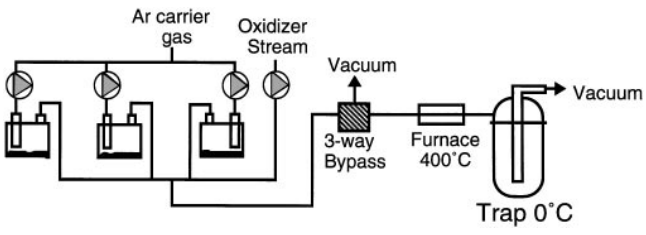

FIG. 3. Schematic of the apparatus employed to trap metal-organic by-products produced from $Ba(hfa)_2$•mep, $Ca(hfa)_2$•tet, and $Cu(dpm)_2$ in MOCVD growth experiments.

in a gold foil pouch to minimize Tl_2O loss as shown in Fig. 4. This pouch was then placed in a quartz tube furnace for open-flow annealing. The atmosphere of the furnace was purged with extra dry grade O_2, 10% O_2/Ar, or Ar before the pouch was sealed. The exit gas flow was passed through an oil bubbler to trap Tl_2O_3 particulate powder and maintain ambient pressure. The temperature was first ramped slowly at 2 °C/min to 700 °C to drive off any absorbed water, then quickly ramped (20 °C/min) to the reaction temperature. Hold times at reaction temperature varied from 0.3 to 15 h. The cooldown employed a ramp to 600 °C at a rate of 1.0 °C/min, and then the furnace was cooled to room temperature over 0.5 h.

F. Thin film characterization

X-ray diffraction θ-2θ and θ rocking curve data were collected with a Rigaku DMAX-A diffractometer using Ni-filtered Cu K_α radiation. In-plane ϕ scans utilized a Troyke 4-circle goniometer with Cu K_α radiation. Film thickness and surface roughness were measured with a Tencor P10 profilometer. A Hitachi 4500 SEM, equipped with a Tracor EDX detector having a light element window and a Cambridge Scientific ZAFS analysis system using internal standards, was utilized to study film morphology and elemental composition. Cross-sectional transmission electron microprobe (TEM) samples were prepared by conventional techniques. Superconducting films were sandwiched between Al_2O_3 single crystal substrates using M-bond 610 epoxy and mounted in 3 mm O.D. stainless steel tubing. Samples were then sliced, ground, and dimpled. Final thinning to perforation was carried out by ion-milling using Ar at 4 kV and liquid N_2 cooling to minimize damage. The TEM studies were carried out on a JEOL 4000EX electron microscope at 400 keV.

Magnetic susceptibility measurements were made using a Quantum Design MPMS SQUID magnetometer. Hysteretic moments were measured with applied fields between −45,000 and 45,000 G. Critical temperature, T_c, and critical current, J_c, data were measured on 80 μm wide patterned bridges using the 4-point probe instrumentation described elsewhere.[68] Transition temperatures (T_c) were also obtained using a noncontact inductive technique. In these measurements, a computer-controlled lock-in amplifier (PAR model 5301) operating at 1.1 kHz was used to monitor the impedance of an inductor coil, placed in close proximity to the sample during a temperature sweep.[69] The transition temperature (T_c) was identified as the temperature at which the imaginary component of the voltage across the inductor began to decrease strongly from the value above the transition. The sample temperature was monitored with a calibrated temperature sensor diode, and the data collected during cooling and warming were in good agreement. For J_c bridges, films were photolithographically patterned using Shipley 1822 positive photoresist and a saturated aqueous EDTA (EDTA = ethylenediaminetetraacetic acid) etchant solution.

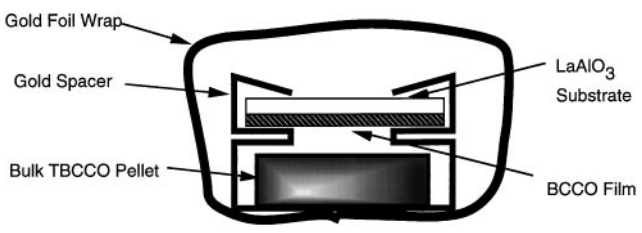

FIG. 4. Diagram of the annealing scheme used to form films of the Tl-2212 superconductor. The large bulk pellet acts as a source for a near-equilibrium vapor pressure of Tl_2O.

Surface resistance measurements were obtained using the parallel plate resonator technique.[70] A 12.5 μm thick piece of Teflon™ (DuPont) was placed between the faces of two Tl-2212 films to form a resonator. The resonator was placed in a sealed cryogenic probe and the assembly was cooled inside a liquid He storage dewar.[71] An HP 8510 Network Analyzer was inductively undercoupled to the parallel plate resonator, and the surface resistance was calculated from the measured quality factor: $R_s = (\pi\mu_0 fs/Q)$ where μ_0 is the permeability of free space ($4\pi \times 10^{-7}$ H/m), f is the resonant frequency, s is the thickness of the dielectric spacer (12.5 micron), Q is the measured quality factor, and R_s is the average surface resistance of the two films. Finally, the surface resistance values were shifted to a comparison frequency of 10 GHz by assuming a frequency squared dependence.

III. RESULTS

A. Metal-organic precursor design and characterization

An effective ligand design strategy to form volatile, monomeric complexes of Ba^{2+} and Ca^{2+} is to saturate the bis(β-diketonate) coordination sphere with polyether ancillary ligands. This strategy was implemented in the qualitatively volatile, thermally stable precursors $Ba(hfa)_2 \cdot$mep and $Ca(hfa)_2 \cdot$tet shown in Fig. 5. However, precursor volatility and thermal stability must be characterized quantitatively and ideally under MOCVD growth conditions. This is accomplished in the present study by measuring the precursor evaporation rate into a horizontal flowing carrier gas under a reduced pressure, using the TGA instrumentation schematically shown in Fig. 1. This vacuum TGA method to measure precursor volatility has not been previously described, and the analysis is discussed in detail below. Typical weight loss and rate of sublimation data [for $Cu(dpm)_2$ in this

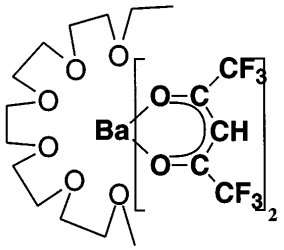

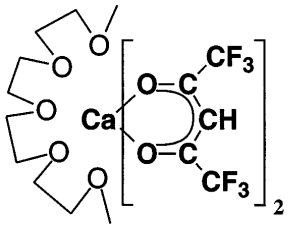

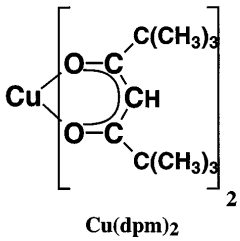

FIG. 5. Precursor molecules utilized in the MOCVD deposition of BaCaCuO(F) thin films. $Ba(hfa)_2 \cdot mep$ (hfa = hexafluoroacetylacetate, mep = methylethylpentaglyme), $Ca(hfa)_2 \cdot tet$ (tet = tetraglyme), and $Cu(dpm)_2$ (dpm = dipivaloylmethanate). The Ba and Ca precursors are liquid under typical film deposition conditions.

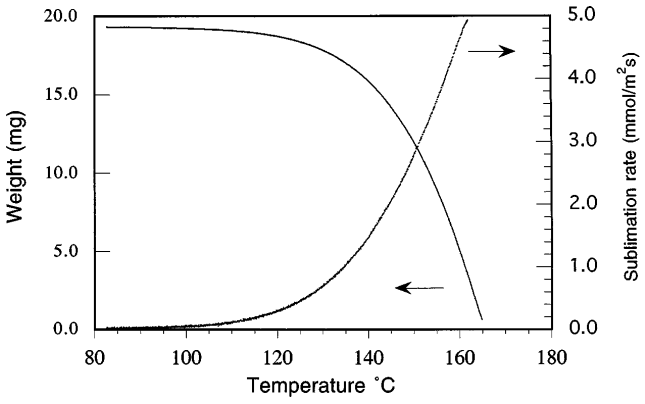

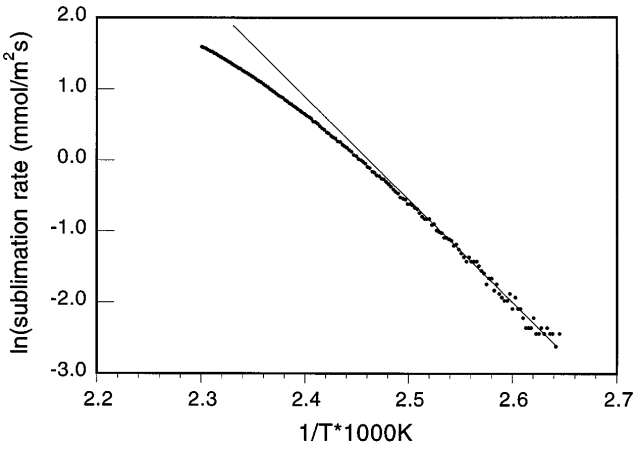

FIG. 6. (a) Typical weight loss and derivative (mass with respect to time) data for the reduced pressure TGA of the MOCVD precursor $Cu(dpm)_2$ at 5 Torr total pressure, N_2 carrier. (b) Arrhenius plot of the sublimation rate versus temperature showing deviation from linearity principally due to diffusion effects (the straight line is drawn as a guide to the eye).

case] are illustrated in Fig. 6(a). The rate of sublimation in (mmol/m^{2}s) is calculated from the derivative of sample weight with respect to time divided by precursor molecular weight and sample pan top cross-sectional area. Figure 6(b) shows an Arrhenius plot of sublimation rate vs $1/T$. Note that at higher temperatures, the data deviate somewhat from linearity. It is unlikely that there is a strong dependence of the enthalpy of sublimation on temperature, and it will be seen that this arises from diffusion effects (*vide infra*). Figure 7(a) shows that for a representative precursor, the rate of evaporation is significantly reduced as the ambient pressure is increased, which indicates that precursor diffusion into the carrier gas stream is a limiting factor in precursor transport. With diffusion effects being important under these conditions, the distance the precursor must travel from the surface of the powder to the crucible top becomes a significant factor in transport rate. Figure 7(b) shows the $Cu(dpm)_2$ evaporation rate as a function of distance from the solid precursor surface to the top of the crucible [x = weight/weight$_{full}$ × crucible height] at constant temperature and pressure. Over a distance of 3.4 mm, a threefold decrease in sublimation rate of $Cu(dpm)_2$ is seen at 5.0 Torr total pressure and 125 °C. The same reduction in evaporation rate as a function of pan height is observed for liquid precursors of similar volatility [e.g., $Ba(hfa)_2 \cdot mep$]. Thus, time-dependent sintering is not the dominant cause of transport rate decline for the powdered precursor.

To model the precursor sublimation rate behavior, the measured weight loss rate is set equal to precursor flux from the top of the pan into the horizontally flowing carrier stream (j_x). It is assumed that this rate is proportional to the pressure of precursor in the plane at the top of the pan (P_x) and to the diffusion coefficient (D) [Eq. (1)], where K is a constant dependent on the crucible top place geometry with respect to the carrier stream using a two-film description.[72] At

$$j_x = KDP_x\,, \qquad P_x = j_x/KD\,, \tag{1}$$

low temperature ramp rates, steady-state conditions should obtain and j_x will equal the flux of precursor from the surface of the powder to the top of the pan. This flux is described by Fick's first law of diffusion

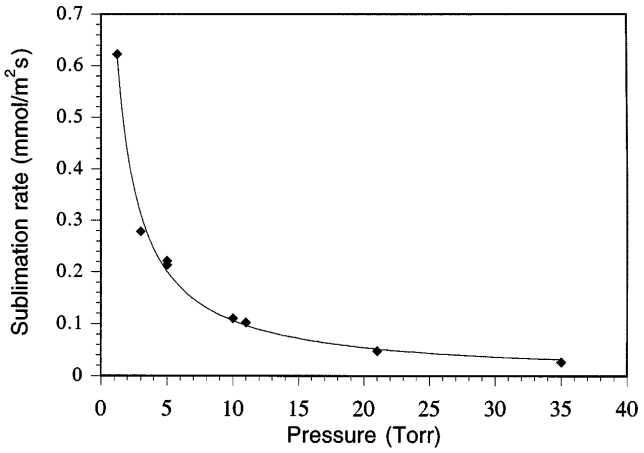

FIG. 7. (a) The effect of system pressure on the sublimation rate of $Cu(dpm)_2$ at 125 °C in a reduced pressure TGA experiment. The line through the data points is drawn as a guide to the eye. (b) Sublimation rate of $Cu(dpm)_2$ as a function of diffusion distance x at 125 °C with 5 Torr N_2 total pressure. Diffusion distance calculated from $\text{weight}_{\text{sample}}/\text{weight}_{\text{full}} \times$ pan height. The solid line is a two-parameter fit of the data points to Eq. (3).

[Eq. (2)]. Substituting P_x from Eq. (1) into Eq. (2) yields Eq. (3), where P_E is the precursor equilibrium vapor pressure at the surface of the powder, and x is the distance from

$$j_x = \frac{D}{x}\,(P_E - P_x)\,, \tag{2}$$

$$j_x = \frac{D}{x}\left(P_E - \frac{j_x}{KD}\right) = \frac{DP_E}{x + 1/K}\,, \tag{3}$$

the powder surface to the top of the pan. A two-parameter fit of experimental j_x vs x data yields the product DP_E and K. The solid line in Fig. 7(b) shows a two-parameter fit to Eq. (3) for the $Cu(dpm)_2$ sublimation data. This single experiment cannot deconvolute intrinsic vapor pressure and diffusion effects. However, from the known equilibrium vapor pressure of $Ba(hfa)_2 \cdot tet$ determined by manometric measurements,[61] the resulting diffusion coefficient for this complex is calculated from DP_E to be 1.5×10^{-2} m^2/s at 115 °C, 5 Torr N_2. To correct for diffusion effects as the sample height changes during the temperature ramp, evaporation rates can be normalized to a constant diffusion distance (chosen as 50% of the pan height, 1.7 mm) using Eq. (4), where R_{dc} is the diffusion-corrected evaporation rate ($mmol/m^2S$), R_{obs} is the observed evaporation rate, w is the sample weight, and w_i is the initial sample weight. This correction factor is a linear approximation of the curve in Fig. 7(b),

$$R_{dc} = \frac{R_{obs}}{11.1\,\frac{w}{w_i} + 0.45}\,, \tag{4}$$

which can be applied to diffusion distances of 1.0–3.0 mm. Errors in estimated sublimation rate from this approximation are $\sim \pm 5\%$ at diffusion distances of 1.0–3.0 mm. This treatment yields approximately linear Arrhenius plots of $\ln(R_{dc})$ vs $1/T$ (Fig. 8). Significant diffusion effects can also be seen in the magnitude of slopes of Arrhenius plots for $Ba(hfa)_2 \cdot tet$ which yield activation energies for the sublimation process at various pressures. These fall drastically as pressure is decreased, as Table II shows. Since diffusion coefficients are generally thermally activated, the apparent activation energy for the sublimation process would be expected to be the sum of the intrinsic vaporization enthalpy and diffusion activation energy terms. As seen in Table II, these values are incrementally higher than the enthalpy of vaporization as measured in a static equilibrium experiment. Thus, at higher total pressures the sensitivity of the precursor sublimation rate to temperature is greater due to diffusion effects.

The relative volatilities of some common HTS MOCVD precursors expressed in terms of Arrhenius plots for sublimation are shown in Fig. 8. Corrections for diffusion effects from sample height during heating are made using Eq. (4). Inflections in slopes are due to precursor melting. Note that fluorinated $Ba(hfa)_2 \cdot tet$ and $Ba(hfa)_2 \cdot mep$ sources are far more volatile than $Ba(dpm)_2$, and that they sublime at temperatures far below the respective decomposition temperatures. For example, $Ba(hfa)_2 \cdot mep$ exhibits an evaporation rate of 0.14 $mmol/m^2s$ at 116 °C while commonly used $Ba(dpm)_2$ requires a temperature of 200 °C to achieve the same sublimation rate at 5 Torr total N_2 pressure.

To demonstrate the stability of $Ba(hfa)_2 \cdot mep$ and $Ba(hfa)_2 \cdot tet$ vapor pressure characteristics compared to those of $Ba(dpm)_2$, evaporation rates were measured (including a diffusion distance correction) over the course of 4.0 days at typical precursor temperatures used in HTS film growth. The TGA chamber was backfilled to

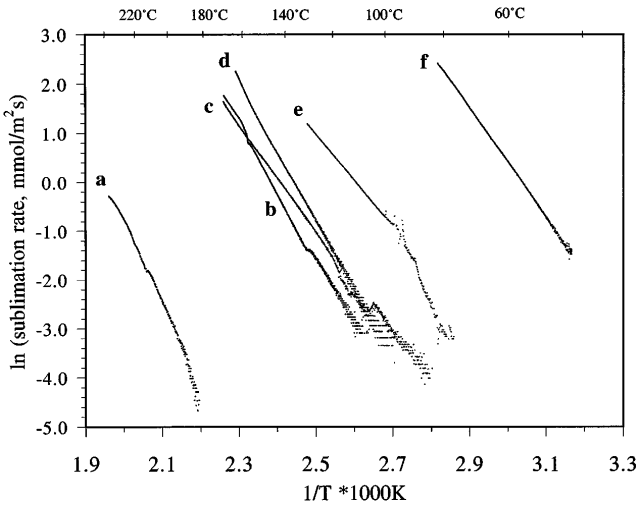

FIG. 8. Comparison of volatilities of several common MOCVD precursors in reduced pressure TGA experiments. Evaporation rates are adjusted to a diffusion distance of 1.7 mm in 5 Torr total pressure N_2. (a) $Ba(dpm)_2$, (b) $Ba(hfa)_2 \cdot tet$, (c) $Ba(hfa)_2 \cdot mep$, (d) $Cu(dpm)_2$, (e) $Ca(hfa)_2 \cdot tet$, and (f) $Cu(hfa)_2$.

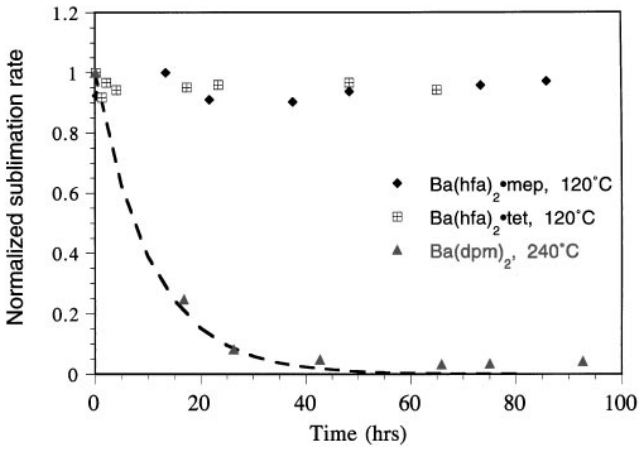

FIG. 9. Reduced pressure TGA sublimation rate stability data for $Ba(hfa)_2 \cdot mep$ and $Ba(hfa)_2 \cdot tet$ compared to commonly used Ba MOCVD precursor $Ba(dpm)_2$. The sublimation rate is measured at 5 Torr total pressure with samples at the indicated temperatures and adjusted for diffusion distance. Between data points, the TGA instrument was backfilled with 1.0 atm of N_2, resulting in negligible sublimation. The curve shown is an exponential fit to the $Ba(dpm)_2$ data points.

TABLE II. Pressure dependence of the evaporation rate activation energy for $Ba(hfa)_2 \cdot tet$ as measured by reduced pressure thermogravimetic analysis. Values from this dynamic method are incrementally higher than those from static equilibrium measurements. The measured activation energy for this process is the sum of the enthalpy of vaporization and the diffusion activation energy.

Total TGA pressure (Torr)	Observed activation energy of evaporation process (kJ/mol)
6.0	118 ± 5
5.0	108
4.0	104
0.1	85
ΔH_{evap} [a]	75

[a]Ref. 61.

atmospheric pressure with purified N_2 between measurements to minimize weight loss (since the diffusion of the precursor at atmospheric pressure is negligible). As is readily apparent in Fig. 9, the fluorinated alkaline earth precursors have much improved vapor pressure temporal stabilities over $Ba(dpm)_2$, which decomposes substantially over the course of 20 h. A fit to the $Ba(dpm)_2$ sublimation rate data is approximately exponential with a half-life of ~9.4 h, while $Ba(hfa)_2 \cdot mep$ exhibits negligible decay (<5%) within the reproducibility of the measurement over a period of 85 h at 120 °C.

B. MOCVD film growth and deposition mechanism

With MOCVD precursors having stable vapor pressures, as demonstrated by reduced pressure TGA characterization studies, it is possible to grow BaCaCuO(F) thin films in a controlled manner and to study the growth mechanism. Of particular interest is defining the kinetics of BaCaCuO(F) film deposition utilizing these novel precursors and ascertaining whether deposition is limited by precursor mass transport or by adsorbate molecule decomposition. In many MOCVD processes, the rate of deposition is limited by transport of the precursor to substrate, not by the kinetics of decomposition of the chemisorbed species.[62,73–75]

To determine if the kinetics are mass transport-limited, it is necessary to consider the relationship of precursor partial pressure to film deposition rate. For simplicity and initial exclusion of precursor synergistic effects, a study of BaF_2 deposition rate as a function of precursor partial pressure for $Ba(hfa)_2 \cdot mep$ alone was undertaken (Fig. 10). As the carrier flow through the $Ba(hfa)_2 \cdot mep$ precursor reservoir is increased from 0 to 150 sccm (with constant total carrier flow over the reaction zone), the BaF_2 deposition rate increases with carrier flow to the 0.7 ± 0.05 power as indicated by the solid least-squares line. This result is consistent with a simple mass transport model of horizontal turbulent flow over a subliming solid precursor. Here a 0.8 power dependence of precursor transport on carrier flow would be expected.[72] Thus, inherent to this reservoir geometry is the fact that the carrier stream does not become saturated with an equilibrium pressure of precursor. In previous studies[46] using the same bubbler geometry, the $Ba(hfa)_2 \cdot tet$ weight loss at 115 °C during the MOCVD growth of BaCaCuO(F) films yielded a precursor partial pressure of 0.005 Torr (calculated from carrier volume

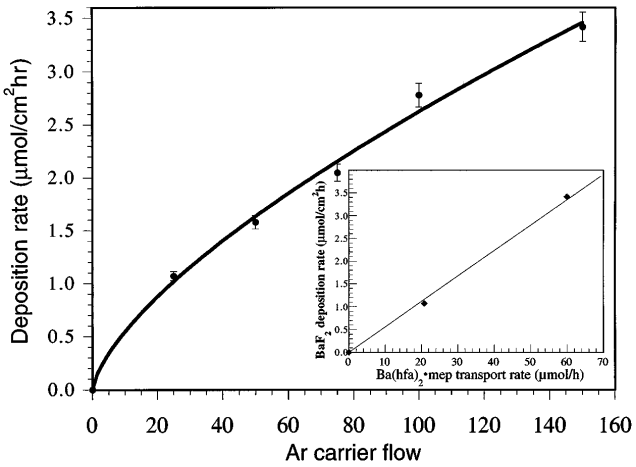

FIG. 10. Dependence of BaF_2 film deposition rate on Ar carrier flow rate over $Ba(hfa)_2 \cdot mep$. The BaF_2 deposition rate increases roughly to the 0.7 power of carrier flow as would be expected for nonequilibrium turbulent mass transfer of precursor into the carrier stream. The inset shows that deposition rate is directly proportional to precursor molar transport rate (as measured by precursor weight loss in reservoir), supporting mass-transport limited deposition kinetics. Deposition conditions: 100 sccm O_2, 250 sccm H_2O, Ar dilution to balance 500 sccm total flow, 5 Torr total pressure, and 720 °C substrate temperature.

and assuming the ideal gas law), far below the equilibrium pressure of 0.2 Torr.[61] Similar precursor dilution effects resulting in nonequilibrium carrier concentrations are discernible in the results of other HTS MOCVD studies in which precursor transport rate and carrier flow data are reported.[58,63,76] Although the carrier stream is not saturated in the present configuration, it is possible to control precursor evaporation rate and thereby demonstrate that deposition rate is proportional to the metal-organic precursor gas phase concentration. The concentration of precursor (C_{prec}) in the reactant stream is simply described by Eq. (5) where dn/dt is the molar transport rate and ν_{total} is the total reactant carrier flow. The inset of Fig. 10 shows that the

$$C_{\text{prec}} = \frac{dn/dt}{\nu_{\text{total}}} \tag{5}$$

film deposition rate is directly proportional to precursor mass transport rate, and thus directly proportional to precursor concentration [Eq. (5)]. This observation is completely consistent with a mass transport-limited mechanism.

If BaCaCuO(F) film growth is indeed mass transport-limited, then the composition of the deposited film should be the same as that of the gas phase. If it is kinetically limited, varying decomposition reaction rates of each precursor should afford film stoichiometries different from the gas phase. We exclude the unlikely possibility that each precursor exhibits nearly identical kinetic behavior. Table III shows that the gas phase Ba–Ca–Cu stoichiometry as measured by precursor weight loss is, within experimental error, identical to that of the deposited film as measured by ICP analysis, supporting a mass transport-limited process.

In the mass transport-controlled deposition regime, the film growth rate should be a sensitive function of the total gas carrier velocity. Figure 11 shows the effect of increasing total reactor pressure (with total reaction carrier gas at constant mass flow, thus decreasing velocity) on the BaF_2 growth rate. The film growth rate dramatically decreases at pressures above 6 Torr. Shown as a comparison is the dependence of precursor TGA sublimation rate on total pressure which parallels but is much less pronounced than the dependence of film deposition rate on total pressure. As pressure is increased, with constant reactant stream mass flow, the total reaction stream velocity decreases, and thus the supply of precursor to reaction zone decreases. Hence, a large decrease in deposition rate is expected and is observed. Also, at lower reaction stream velocities (higher pressures), the uniformity of deposition is compromised

TABLE III. Comparison of gas phase metal stoichiometry, as determined by precursor weight loss from the individual evaporators, and film metal stoichiometry as determined by ICP analysis for the MOCVD growth of BaCaCuO(F) films. A mass transport-limited reaction would require the stoichiometries to be the same as is observed within the precision of the measurements.

	Ba : Ca : Cu
Gas phase	35 : 25 : 41
Film	34 : 24 : 42

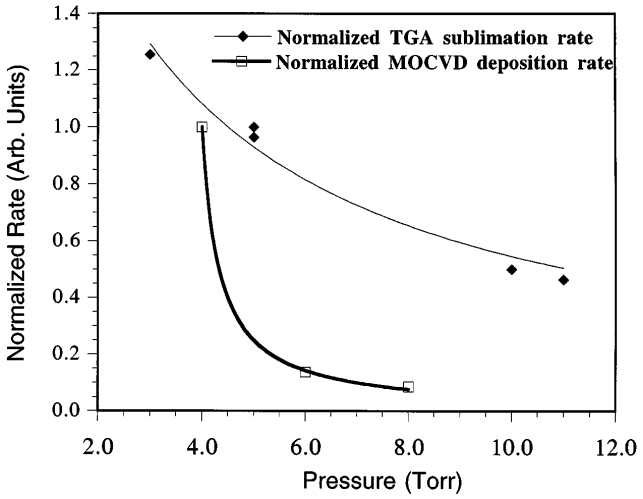

FIG. 11. Deposition rate of BaF_2 films versus system pressure showing the large effect of carrier velocity on film deposition rate. Pressure is regulated by throttle valve on the reactor exhaust. Conditions: 500 sccm total flow and 500 °C substrate temperature. For comparison, normalized TGA evaporation rate data for of $Ba(hfa)_2 \cdot mep$ at 120 °C as a function of pressure are shown.

by thermal buoyancy effects perturbing reactant flow.[73] For the present precursor volatilities and flow rates, it is found that operating pressures of less than 5 Torr are necessary for uniform BaCaCuO(F) growth at useful growth rates (>20 nm/min).

In a mass transport-limited process, the deposition rate is only moderately dependent on temperature, and there exists a temperature below which the kinetics of precursor decomposition become rate-limiting.[73–75] Thus, it is of interest to examine the BaCaCuO(F) deposition rate versus substrate temperature for the present precursors and reactor design, with the data shown in Fig. 12. In this film growth experiment, the gaseous precursors $Ba(hfa)_2 \cdot mep$, $Ca(hfa)_2 \cdot tet$, and $Cu(dpm)_2$ were mixed with an $O_2 + H_2O$ oxidizer stream mixture under the conditions shown in Table I. Note that a transport-limited growth regime begins at temperatures above 350 °C for BaCaCuO(F) film growth [Fig. 12(a)]. In principle, the effect of H_2O on the decomposition of these precursors may be significant since it could act as a protonolytic reagent to form volatile Hhfa by-products.[77–79] To explore this possibility, the above experiment was conducted without water in the oxidizing stream. The same general results were observed with mass transport-limited deposition of Ba and Ca beginning near 400 °C [Fig. 12(b)]. The deposition characteristics of $Cu(dpm)_2$ under the conditions of Fig. 12(b) are, however, markedly different. At 400 °C, there is essentially no Cu deposition. A possible explanation is that the decomposition of $Ba(hfa)_2 \cdot mep$ and $Ca(hfa)_2 \cdot tet$ forms free or chemisorbed Hhfa which then transports (etches) Cu from the film as in Eq. (6).[77,80,81]

$$Ba(hfa)_2 \bullet mep + CuO_{surface} \longrightarrow Cu(hfa)_2 + mep + BaO_{surface}\,. \quad (6)$$

For substrate temperatures of 500–800 °C, the Cu deposition rate increases gradually. This is consistent with the etching process of Eq. (6), if at higher temperatures the subsequent decomposition of Hhfa or of $Cu(hfa)_2$ to CuO eliminates the etching pathway. The temperature versus deposition rate plot for $Cu(dpm)_2$ alone in Fig. 12(c) evidences a constant growth profile with film growth rate gradually increasing with increasing temperature. Clearly the abatement of CuO deposition at 400 °C seen in Fig. 12(b) requires the presence of fluorinated precursors $Ba(hfa)_2 \cdot mep$, $Ca(hfa)_2 \cdot tet$, and the absence of H_2O.

To test further the hypothesis that Cu can be removed from BaCaCuO(F) films as $Cu(hfa)_2$, the volatile metal-organic by-products of the reaction $Ba(hfa)_2 \cdot mep + Ca(hfa)_2 \cdot tet + Cu(dpm)_2$ under codeposition conditions were trapped at 0 °C after passing the gaseous mixture through a quartz tube at 400 °C (as in Fig. 3). The trapped solid products were

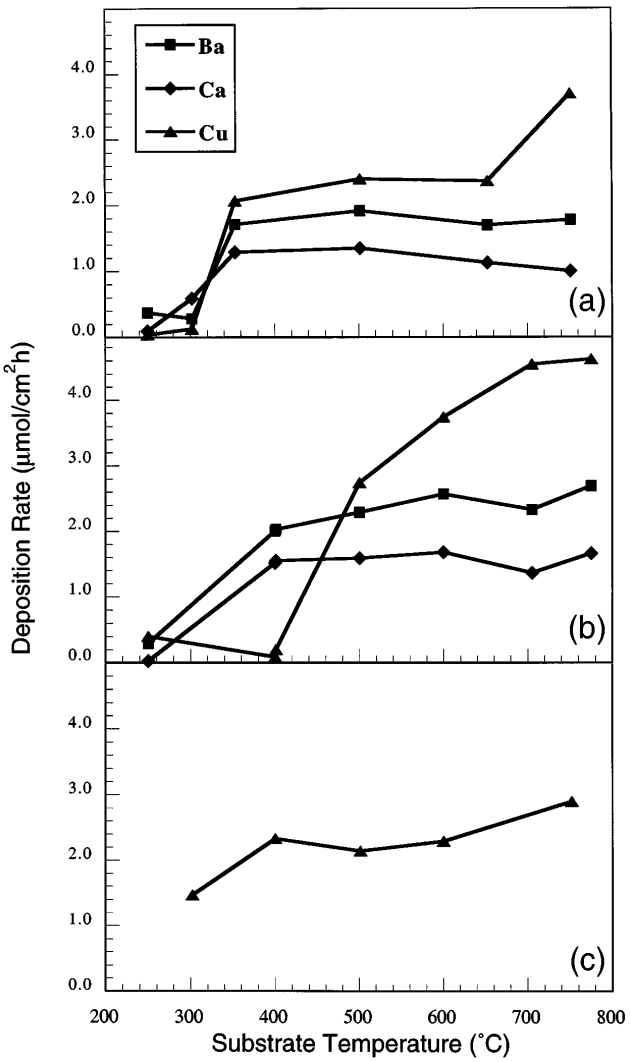

FIG. 12. Deposition rate of BaCaCuO(F) films versus substrate temperature showing the onset of mass transport-limited kinetics for the precursors $Ba(hfa)_2 \cdot mep$, $Ca(hfa)_2 \cdot tet$, and $Cu(dpm)_2$. Mass transport-limited growth begins as low as temperatures ~350 °C. Ar carrier flow of 150 sccm, constant total carrier flow of 500 sccm, total pressure 5 Torr; metal content measured by ICP analysis. (a) Oxidizer stream of 100 sccm O_2 + 250 sccm H_2O. (b) Oxidizer stream 350 sccm O_2. (c) $Cu(dpm)_2$ deposition only with an oxidizer stream of 350 sccm O_2.

then analyzed by mass spectrometry (see Experimental Section for data). When the products of the MOCVD reaction at 400 °C *without* H_2O in the oxidizer stream [as in Fig. 12(b)] were analyzed, both $Cu(hfa)_2$ and Cu(hfa)(dpm) were observed under conditions where CuO etching was prevalent. For the same experiment *with* H_2O in the oxidizer stream [as in Fig. 12(a)], $Cu(hfa)_2$ and Cu(hfa)(dpm) were also observed (without lowering of CuO deposition). Thus, trace ligand exchange is operative without simultaneous suppression of CuO deposition. The formation of mixed β-diketonate ligand complexes such as Cu(dpm)(hfa) is not surprising

and has been observed in solution exchange experiments with Cu^{2+} β-diketonates.[82] It is important to note here that in control experiments, no $Cu(hfa)_2$ is detected in trapped products from the carrier stream that did not pass through a hot reaction zone. Thus, detection of $Cu(hfa)_2$ is not an artifact of the mass spectrometry experiment, nor is ligand exchange prevalent in the carrier stream at 150 °C. Exchange of polyether ligands in $Ba(hfa)_2 \cdot mep + Ca(hfa)_2 \cdot tet$ is evidenced by the mass spectrometric observation of $[Ba(hfa) \cdot tet].^+$ When freshly synthesized powders of $Ba(hfa)_2 \cdot mep$ and $Ca(hfa)_2 \cdot tet$ are mixed and introduced into the mass spectrometer, this polyether exchange is also observed. Thus, we cannot distinguish between polyether ligand exchange in the carrier stream or as an artifact of the mass spectrometry experiment.

C. BaCaCuO(F) film deposition process

Although the present MOCVD process is chemically complex, thin films of uniform composition over relatively large substrate areas can be readily grown. The conditions for the growth of BaCaCuO(F) films with a 2 : 1 : 2 Ba : Ca : Cu cation stoichiometry are given in Table I. The present simple, modular reactor design affords a uniform deposition rate of 20 nm/min with ±5% variation in measured thickness over a 16 cm^2 area. Randomly oriented crystalline phases of BaF_2, CuO, Ca_2CuO_3, and $BaCu_2O$ are observed[83] in the deposited films by x-ray diffraction (Fig. 13).

As a consequence of using fluorine-containing metal-organic precursors, BaF_2 is readily incorporated in the films. To reduce the fluoride content, H_2O is added to the oxidizer stream to remove fluorides, presumably as volatile HF. It was found that relatively high deposition temperatures (780 °C) are required to remove all fluorides *in situ*. Figure 14 shows thin window EDX data for BaCaCuO(F) films grown between 733 °C and 780 °C with H_2O in the oxidizer gas stream. It can be seen that fluorides are readily removed at film growth temperatures approaching 780 °C, presumably as in Eq. (7).

$$BaF_2 + H_2O \longrightarrow BaO + 2HF. \qquad (7)$$

The films deposited at higher temperature have high crystal growth rates, resulting in rough morphological features. This is illustrated in the scanning electron micrograph of Fig. 15(a) showing large, multimicron-sized features. These features correlate with a large segregation of elements seen in SEM/EDX analysis of various grains. This yields variations (standard deviation of ±30%) in metal stoichiometry from the desired 2 : 1 : 2 ratio. At lower growth temperatures, a higher nucleation rate is observed, and the film morphology is markedly smoother, having features on the order of 0.1 μm [Fig. 15(b)]. Here the stoichiometry of the various grains is identical to within the resolution of the SEM/EDX experiment. Thus, BaCaCuO(F) films are

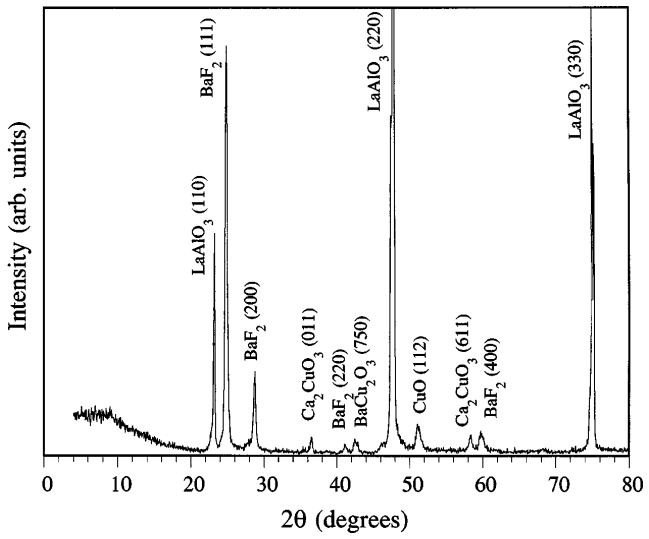

FIG. 13. θ-2θ x-ray diffraction scan of a BaCaCuO(F) film grown on (110) $LaAlO_3$ under conditions given in Table I.

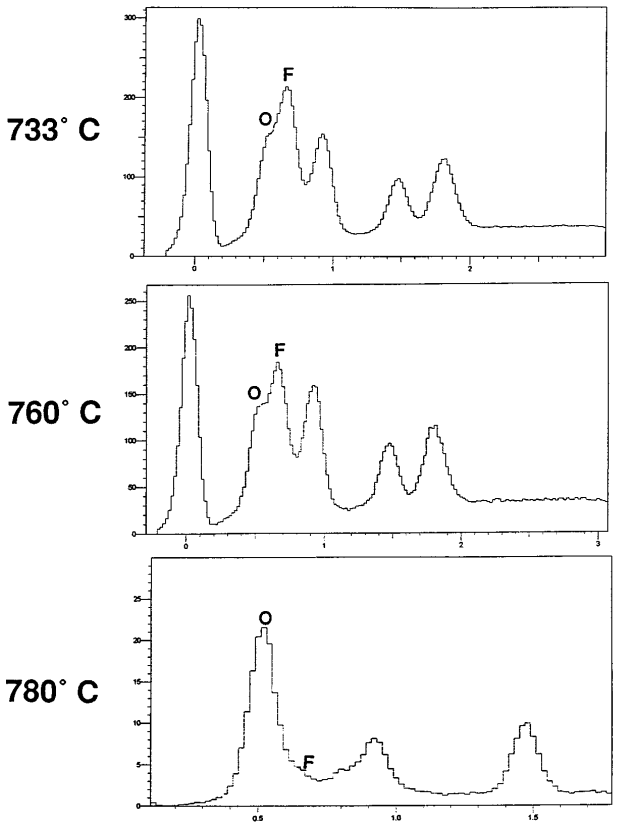

FIG. 14. Windowless EDX spectra showing BaCaCuO(F) film fluoride content at the film growth temperatures indicated. Growth conditions: 150 sccm Ar carrier, 100 sccm O_2, 250 sccm H_2O, and 5 Torr total pressure.

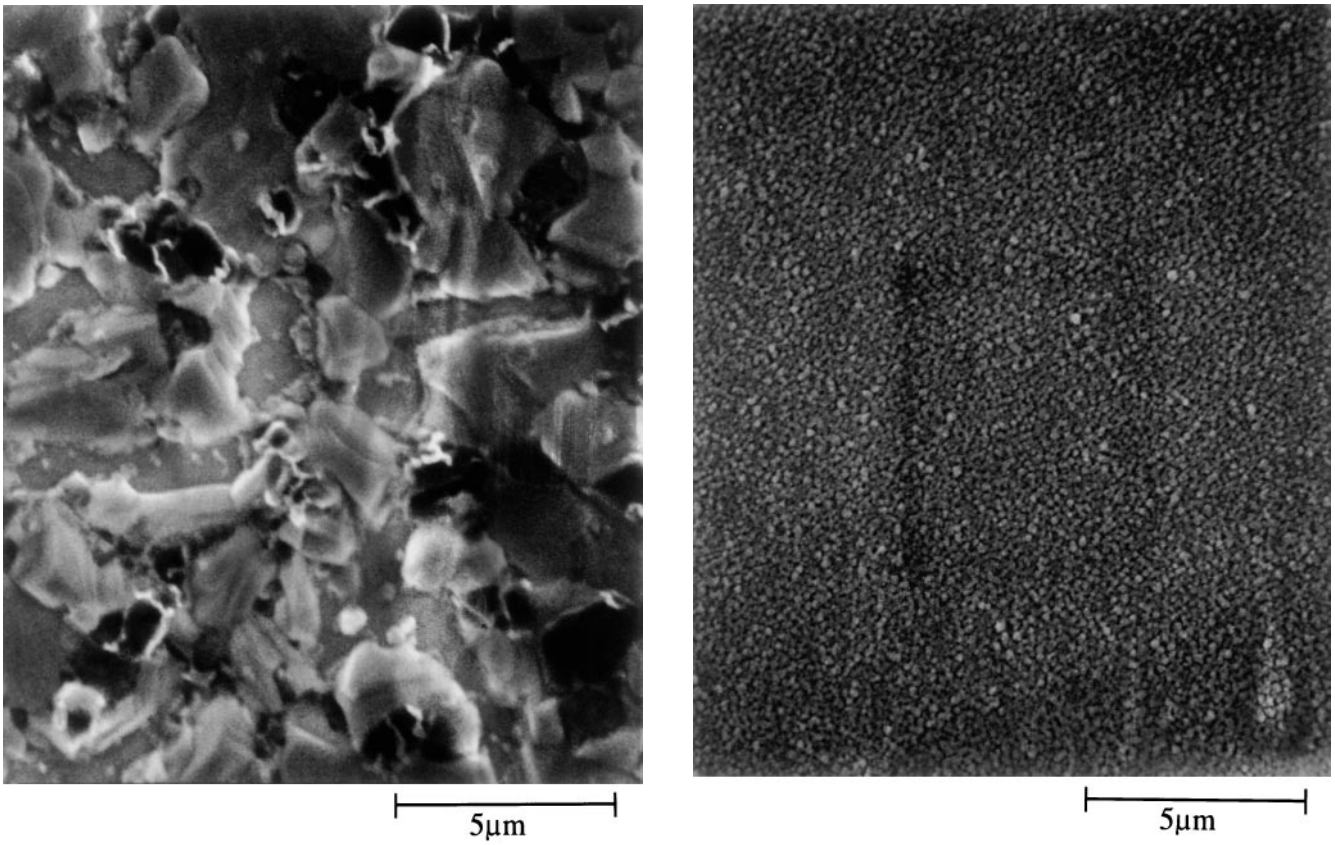

FIG. 15. (a) SEM image of a fluorine-free, MOCVD-derived BaCaCuO film deposited at a substrate temperature of 780 °C showing rough surface morphology. (b) SEM image of the surface morphology of a BCCO(F) film grown on (110) $LaAlO_3$ under typical MOCVD deposition conditions with a 500 °C substrate temperature.

grown at lower temperatures to achieve smoother morphology and greater film compositional homogeneity.

D. Tl-2212 phase formation

In the present study, BaCaCuO(F) precursor films were annealed over a $Tl_2O_3:BaO:CaO:CuO$ (1:2:1:2) pellet at various O_2 pressures and at temperatures between 720 and 895 °C to form the superconducting Tl-2212 (see Sec. II for details). It was found that phase-pure Tl-2212 is produced more efficiently at annealing temperatures of 875, 820, and 720 °C in atmospheres of 100, 10, and 0% O_2, respectively. For annealing in 100% O_2, the temperature window to form phase-pure Tl-2212 is ±20 °C, with a mixture of Tl-2212/1212 phases being formed outside of this temperature window. The heating profile is also important in obtaining highest film quality with slow temperature ramps (2 °C/min) to 700 °C being optimum. Films processed in this manner are shiny to the eye, and the surface morphology is dominated by evidence of a melt during phase formation as shown in Fig. 16(a). Large, smooth platelets of ~20 μm dimensions and 50 nm step heights are seen by profilometry. Figure 16(b) shows a profilometry profile of the sample shown in Fig. 16(a). Typical rms values of the surface roughness are 100 nm which result from small grains of non-*c*-axis aligned material growing on the *c*-axis oriented crystal surface. On top of the platelets, the crystal is very smooth with rms roughness values as low as 20 Å. As annealing temperatures are reduced, surface morphology becomes smoother. In Fig. 16(c), the rms roughnesses of Tl-2212 films (over a 200 μm scan length) are shown as a function of annealing temperature. At annealing temperatures below 860 °C in O_2, a noted improvement in film smoothness to under 10 nm rms roughness is seen.

It is important to note that no fluoride-containing phases are detected by windowless EDX, Auger analysis (<0.1% resolution), nor by XRD in Tl-2212 films produced from MOCVD-derived BaCaCuO(F) films grown at 500 °C. Residual fluoride is presumably removed during the anneal as TlF, which is volatile and thermodynamically favored with respect to Tl_2O_3.[84–86] Thus,

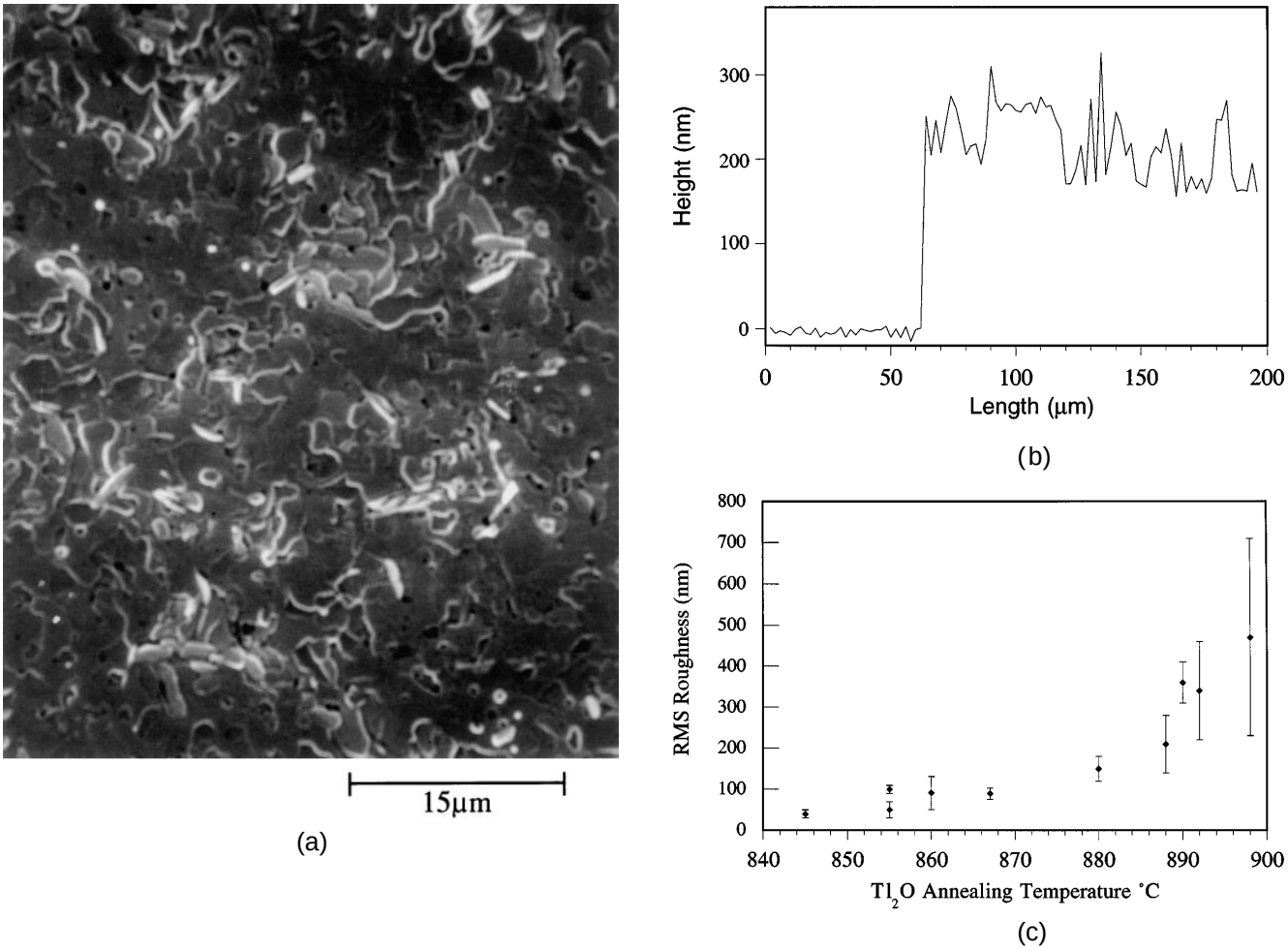

FIG. 16. (a) SEM image of a MOCVD-derived Tl-2212 film grown on (110) $LaAlO_3$ showing platelet structure. (b) Corresponding profilometry scan of the same film showing an rms roughness of 200 Å (the first 50 μm of the scan corresponds to bare $LaAlO_3$ substrate from the photolithographically patterned film). The smooth plates typically have rms roughness of ~20 Å. (c) Plot of surface rms roughness versus film annealing temperature showing a marked increase in smoothness at lower annealing temperatures. Error bars represent the standard deviation of five different scans on the same sample at different random locations.

the overall reaction can be described as in Eq. (8). This efficient removal of fluorides allows the use of fluorinated metal-organic precursors at lower deposition temperatures.

$$Ba_2CaCu_2O_{5-y/2}F_{y(\mathrm{film})} + (1 + y/2)Tl_2O_{(g)} + O_2 \longrightarrow Tl_2Ba_2CaCu_2O_{8(\mathrm{film})} + y\mathrm{TIF(g)}\,. \quad (8)$$

E. Tl-2212 film characterization

To characterize the microstructure of the MOCVD-derived Tl-2212 films, x-ray diffraction techniques were first employed. A θ-2θ x-ray diffraction scan [Fig. 17(a)] shows phase-pure Tl-2212 resulting from annealing an MOCVD-derived BaCaCuO(F) film on (110) $LaAlO_3$ substrate with a bulk Tl-2212 pellet at 875 °C. Only (001) reflections are observed. Indicating that the film is highly *c*-axis oriented. A θ-rocking curve (a further measure of *c*-axis orientation) exhibits a full width at half maximum of 0.38° [Fig. 17(b)], which is comparable to values for typical PVD-derived films.[24] An in-plane ϕ-scan [Fig. 17(c)] shows the relative orientation of the cell axes within the *a*-*b* plane. Reflections appear every 90° as expected for an epitaxial, tetragonal TBCCO film. Figure 17(c) also shows the pseudo-cubic {101} reflections of the $LaAlO_3$ substrate with overlapping ϕ angles, thus indicating registry of the Tl-2212 *a*-*b* axes with the substrate pseudo-cubic *a*-*b* axes.

To examine further the epitaxial growth of the present Tl-2212 films, cross-sectional, high resolution TEM was employed. Figure 18(a) illustrates some of the typical features observed in the MOCVD-derived films, namely a film thickness of about 3500 Å, a *c*-axis which is generally perpendicular to the substrate surface plane, and a sharp interface between the substrate and the film.

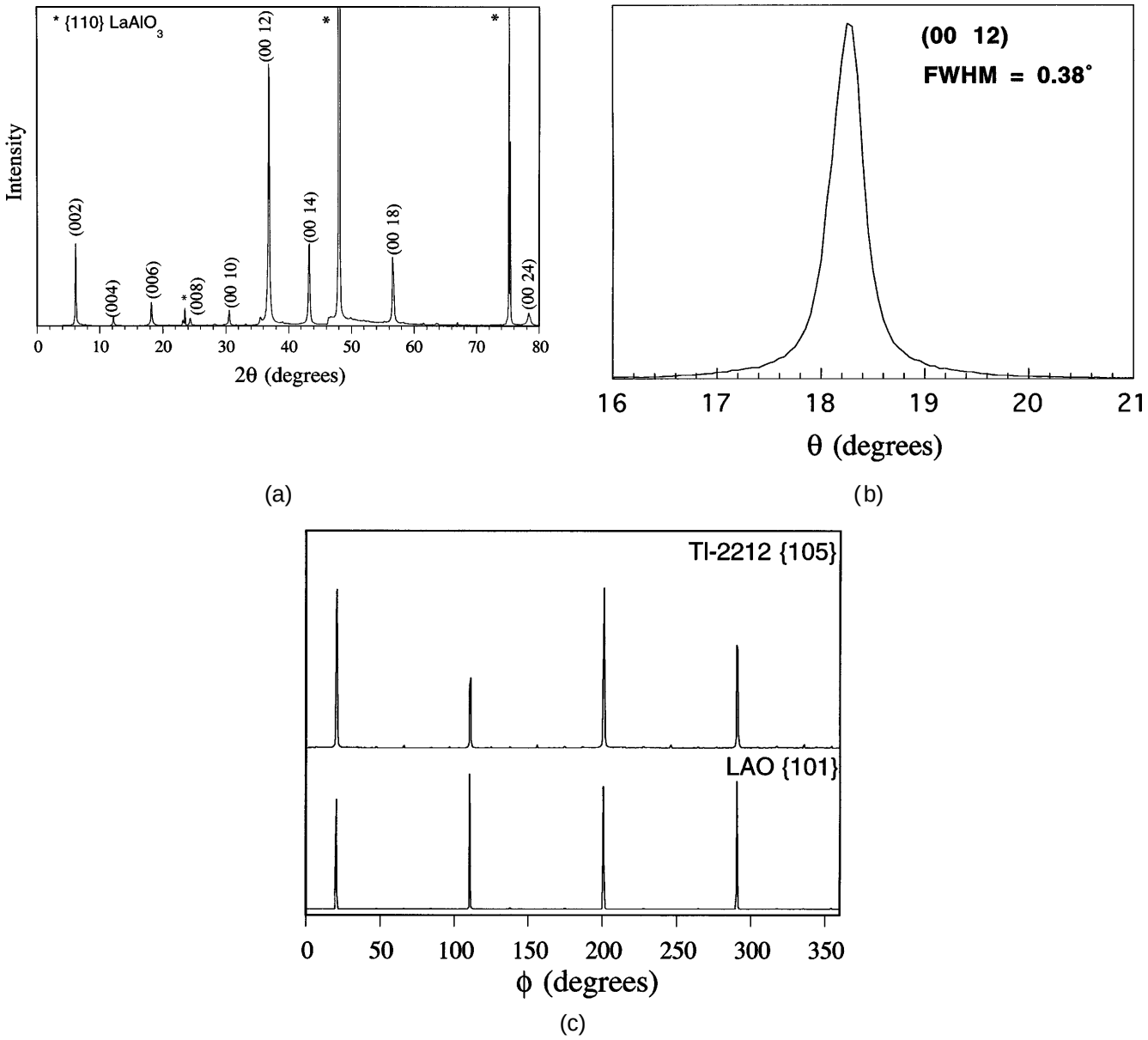

FIG. 17. (a) θ-2θ x-ray diffraction pattern of a MOCVD-derived Tl-2212 thin film grown on (110) $LaAlO_3$. (b) θ-rocking curve of the (0012) reflection of a MOCVD-derived Tl-2212 thin film grown on (110) $LaAlO_3$ [pseudo cubic (100)]. (c) In-plane ϕ-scan of the {105} reflections of a MOCVD-derived Tl-2212 showing alignment with the underlying pseudo-cubic {101} reflections of the $LaAlO_3$ substrate and indicating epitaxial growth.

Some granular features are identifiable in the film by the inhomogeneous image contrast. Usually these features are associated with very small misorientations (one part of the crystal may be tilted a degree or so), but some may also be due to second phases. More significant lattice misorientations between grains in the Tl-2212 film are also observed. A very different orientation is observed for the grain marked by an asterisk (the *c*-axis not parallel to the surface normal). This misoriented growth corresponds to the large features seen in profilometry measurements. There is no evidence of any correlation between the misoriented grains in the film and the microstructure and morphology of the substrate. Strain field contrast is seen at the Tl-2212 interface with periodicity of about 200 Å, in agreement with the non-negligible lattice mismatch between the Tl-2212 film and the $LaAlO_3$ substrate. The lattice mismatch can be distinguished directly in the corresponding selected-area electron diffraction (SAED) pattern shown in Fig. 18(b).

In Fig. 18(b), reflections arising from the $LaAlO_3$ substrate are marked by black dots. Based on the pseudo-cubic perovskite structure for $LaAlO_3$, the orientation

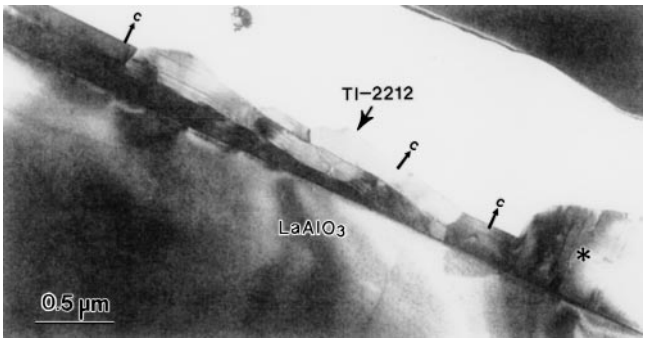

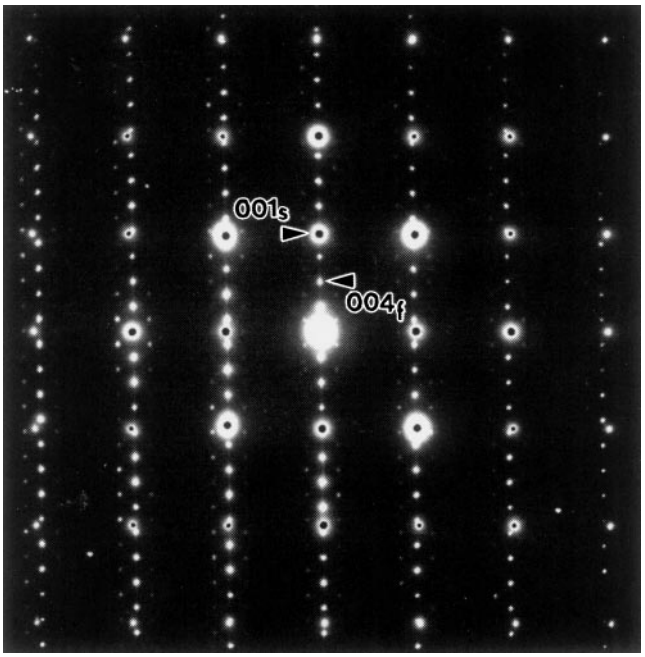

(a) (b)

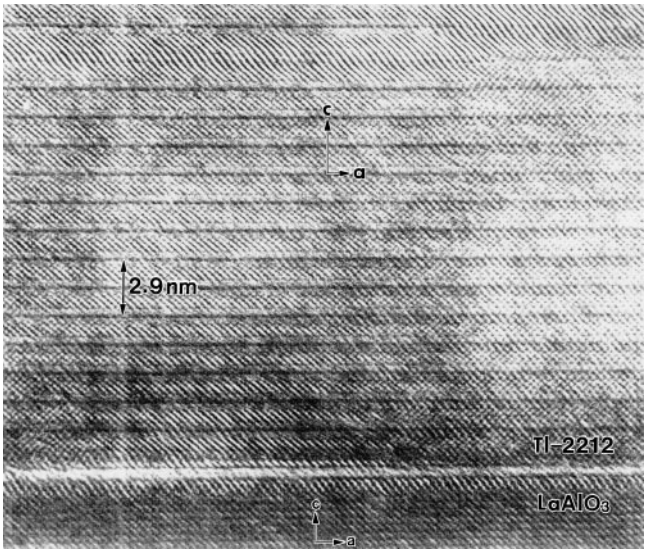

(c)

FIG. 18. (a) Low magnification cross-sectional TEM image showing a Tl-2212 film with the *c*-axis normal to the $LaAlO_3$ the surface. Low angle grain boundaries are observed as indicated by the arrows showing *c*-axis directions for several grains. The region denoted by asterisks (*) contain unaligned Tl-2212 which results in the rough morphology observed by profilometry. (b) Selected area electron diffraction showing crystal orientation of the Tl-2212 film (white spots) with the $LaAlO_3$ substrate (dark spots). (c) High resolution lattice imaging showing an abrupt interface between MOCVD-derived Tl-2212 film and the $LaAlO_3$ substrate.

relationships between the substrate and the film can be described as (001)sub ‖ (001)film and [100]sub ‖ [100]film. The lattice constants can be calculated from the pattern as $a = 3.87$ Å and $c = 29.2$ Å for the Tl-2212 film. The lattice mismatch along the *a*-direction of the substrate is thus calculated as $(df - ds)/ds = 1.67\%$, where df and ds are lattice spacings along the *a*-direction of the film and the substrate, respectively. Satellite reflections appearing around the main Tl-2212 reflections indicate a modulation structure with a superperiod of $5.9a$ along the *a*-direction. The SAED patterns obtained from

various areas of the film confirm Tl-2212 as the major phase in the films, although a rather high density of stacking faults is observed in some areas.

Figure 18(c) shows a high-resolution electron microscopy (HREM) image of another area of the film. The Tl-2212 structure can be distinguished for the film, and the substrate/film orientation relationships determined by the SAED patterns can also be verified. The substrate/film interface is abrupt. However, on this scale an interfacial layer with a severely disordered structure can also be seen. The thickness of this layer is about 4–5 Å, but the origin and identity of the layer has not yet been established. It is also observed from these HREM images that the presence of small steps (a few Å in height) does not disrupt the epitaxial growth of the Tl-2212 films.

High resolution energy-dispersive x-ray spectroscopy (EDS) was performed to look for interdiffusion at the interface. Diffusion of Al into the films was detected in some but not all interfacial areas. Our preliminary analyses suggest an Al content of ~1 at.% near the interface, based on a normalization with the Cu signal. No La signal was observed in these spectra, so it is unlikely that this is a spurious signal from the substrate.

Transport measurements provide further indications of film properties. The resistance versus temperature behavior of a MOCVD-derived Tl-2212 film grown in the present study [Fig. 19(a)] indicates $T_c = 103$ K. Shown in Fig. 19(b) is an inductive T_c measurement on a Tl-2212 film revealing a sharp transition, and supporting Tl-2212 phase purity, i.e., showing no response from intergrowths of the lower T_c Tl-1212 phase. Several films were patterned using standard photolithography and EDTA etching to define an 80 μm wide microbridge structure. Critical current density results from dc and pulsed transport measurements at fixed temperature appear in Fig. 20. At 77 K, the highest $J_c = 1.2 \times 10^5$ A/cm^2, as defined by a 10 μV/cm offset criterion. A Bean model analysis[87] using magnetic hysteresis data yields $J_c = 6.2 \times 10^6$ A/cm^2 at 5 K ($H = 0$ T) and 6.3×10^5 A/cm^2 at 77 K ($H = 0$ T). Figure 21 shows surface resistance data from two Tl-2212 films, performed in a parallel plate resonator configuration. This measurement yields $R_s = 0.40$ mΩ at 5 K, 10 GHz, which is suitable for microwave applications.

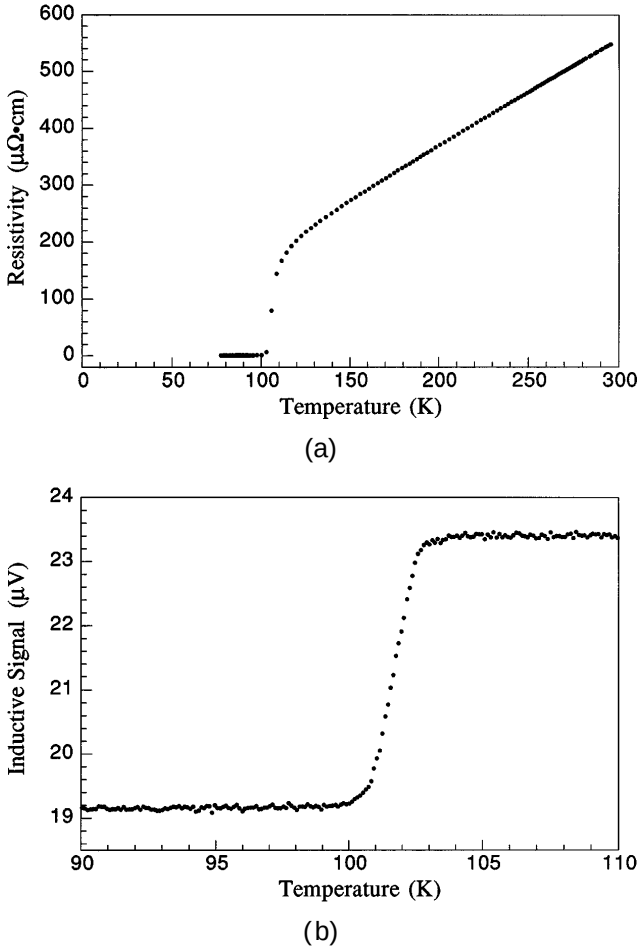

FIG. 19. (a) Variable-temperature, four-probe resistivity data for a MOCVD-derived Tl-2212 film showing $T_c = 103$ K. (b) An inductive T_c measurement on a Tl-2212 film showing a sharp critical transition through the sample.

IV. DISCUSSION

A. Metal-organic precursor design and characterization

Efficient MOCVD processes rely critically on the availability of high purity metal-organic precursors with high, stable vapor pressures. An efficacious approach to such precursors is to minimize molecular oligomerization by saturating the metal coordination sphere with sterically hindered and/or fluorinated ligands. Of equal importance is that the precursor have suitable reactivity under film deposition conditions and not undergo significant prior gas phase decomposition. With regard to precursor design, β-diketonates form volatile complexes with most metals and offer great chemical versatility. One modification strategy is to use sterically encumbered substituents such as the *t*-butyl groups in the dpm ligand to saturate the metal coordination sphere. However, with large ionic radius dipositive ions such as alkaline earths, the dpm ligand alone is frequently ineffective in saturating the coordination sphere, and thereby also ineffective in reducing lattice oligomerization. Hence, dpm complexes of Ba^{2+}, Sr^{2+}, and Ca^{2+} are seldom monomeric and usually exhibit low volatilities.[51–59] To achieve suitable vapor pressures, these dpm compounds must be heated to near the respective decomposition temperatures, resulting in unstable vapor pressure characteristics and unreliable CVD processes.

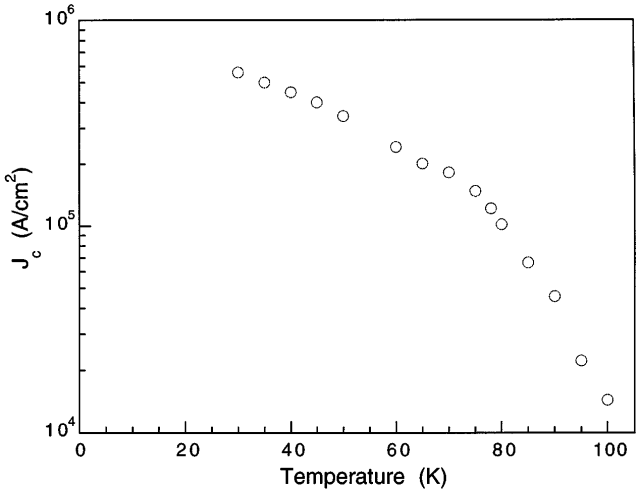

FIG. 20. Transport-measured critical current density as a function of temperature for a MOCVD-derived Tl-2212 thin film. Measurements were performed on a 80 μm wide bridge using a 10 μV/cm criterion.

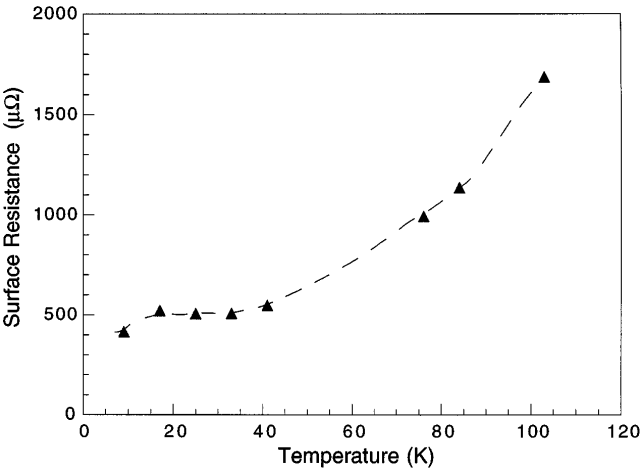

FIG. 21. Temperature dependence of the microwave surface resistance (R_s) of a pair of MOCVD-derived Tl-2212 thin films at 10 GHz as measured by a parallel plate resonator technique.

Another attractive strategy for precursor design is to use electron-withdrawing fluorinated ancillary ligands to reduce van der Waals interactions and to promote the coordination of additional neutral, basic ligands, further saturating the metal coordination sphere. This approach has been successfully applied to complexes such as $Ba(hfa)_2 \cdot tet$, which sublimes as a monomer at temperatures ~100 °C less than does $Ba(dpm)_2$.[45,60] The electron-withdrawing hfa ligand is crucial since polyether adducts of $Ba(dpm)_2$ readily dissociate below the respective sublimation temperatures.[51,61] The fluorinated β-diketonate/polyether adduct class of precursors has been employed in the MOCVD growth of high-quality HTS films.[33,45,88–91] A further improvement has been to lower the melting point since liquid precursors eliminate vapor pressure instabilities arising from sintering-related variations in powder surface area. A successful approach to lowering the precursor melting point has been to modify the coordinating polyether. Using unsymmetrical polyethers, Neumayer *et al.* developed volatile precursors such as $Ba(fha)_2 \cdot$ methylbutylhexaglyme (mp = 52 °C),[64] and the related $Ba(hfa)_2 \cdot$ mep (Fig. 5; mp = 110 °C) which is used as a liquid Ba precursor in the present study. Alternatively, long-chain, fluorinated β-diketonates afford lower precursor melting points as in $Ba(tdfnd)_2 \cdot tet$ (tdfnd = tetradecafluorononanedionate) having mp = 72 °C[92] and demonstrated viability in MOCVD growth processes.[92]

In order to have a controlled MOCVD process, the vapor pressures of the metal-organic precursors must be thoroughly characterized. However, many HTS metal-organic precursors exhibit low vapor pressures (<0.2 Torr under usual deposition conditions), rendering traditional vapor pressure measurements difficult and possibly irrelevant if diffusion effects dominate the transport process. Such vapor pressures are typically measured with a manometer using a rigorously sealed, evacuated chamber.[93] This procedure can incur significant inaccuracies due to formation of decomposition products and other volatile impurities. With great care, reliable data can be obtained[53,61]; however, no information about diffusion effects is obtained. It is thus important to have a convenient and reliable method to compare volatility, diffusion, and stability in a MOCVD environment for newly developed precursors. Evaporation rate measurements are often related to equilibrium vapor pressure by the Knudsen–Langmuir equation [Eq. (9)],[94]

$$j = \alpha P_E (M/2\pi kT)^{1/2} \quad (9)$$

where j is the evaporation rate per unit area, α is the condensation coefficient, P_E is the equilibrium partial pressure, M is the molecular weight, k is the Boltzmann constant, and T is temperature. However for many MOCVD precursors with partial vapor pressures above 10^{-4} Torr, diffusion and surface cooling effects become large, rendering the relation to equilibrium pressure inexact.[93]

There are several recent examples of reduced pressure TGA being used to study the volatility of MOCVD precursors.[52,59,95–97] Takahashi *et al.* used the classic Langmuir relation [Eq. (9)] to describe the volatility of organic monomers for vapor deposition/polymerization.[96] However, the condensation coefficient α for organic powders is difficult to determine without knowledge of the equilibrium vapor pressure and can vary from unity by several orders of magnitude.[98] Chou *et al.* measured dynamic evaporation rates of

$Ba(dpm)_2$, $Ca(dpm)_2$, and $Cu(dpm)_2$ at 20 Torr total pressure, which is near typical low-pressure MOCVD conditions.[52] They reported a decrease in sublimation rate with time, which they attributed to sintering and change in precursor filling height in the sample pans. Diffusion data were not obtained, and the effects of sintering were not discerned from sample preparation effects. Here we report a simple reduced pressure TGA experiment that allows measurement of the product of the diffusion coefficient times the equilibrium vapor pressure of a MOCVD precursor. This allows a comparison of precursor transport characteristics in the MOCVD film growth environment. With the equilibrium vapor pressure of the compound known, the diffusion coefficient can then be estimated.

The observed diffusion effects on precursor sublimation rate in the reduced pressure TGA experiment are significant with a 3-fold decrease for $Cu(dpm)_2$ over a distance of several mm at 5 Torr total pressure [Fig. 7(b)]. The apparent activation energies of vaporization (Table II) similarly show a strong pressure dependence as expected for a diffusion-limited process. Thus, since the sublimation rate is strongly dependent on diffusion, equilibrium vapor pressure data alone cannot be used to find the optimal temperature for a given transport rate in an MOCVD process unless evaporator design (large surface areas with low carrier flow) ensures that equilibrium pressures are obtained. At a given pressure (e.g., 5 Torr in this study), diffusion effects across the sample pan container can be normalized to a constant diffusion distance, and the volatilities of various precursors can be compared under typical MOCVD growth conditions. This comparison provides a gauge for relative precursor volatility, and this information is crucial in selecting precursor conditions for desired growth rate and film stoichiometry. The transport characteristics of several precursors for HTS growth are shown in Fig. 8. The fluorinated $Ba(hfa)_2 \cdot tet$ and $Ba(hfa)_2 \cdot mep$ sources are clearly more volatile than $Ba(dpm)_2$ and sublime at temperatures far below their respective decomposition temperatures. This characteristic is critical for MOCVD process control since a decomposing precursor will produce an unstable vapor pressure, and film stoichiometry will therefore be uncontrollable. Also of interest is that $Ba(hfa)_2 \cdot mep$ is a liquid at typical precursor temperatures (which further aids in growth reproducibility) and exhibits $\sim 3\times$ the volatilization rate of $Ba(hfa)_2 \cdot tet$ at 120 °C.

High precursor volatility is important, but also critical is the demonstration of long-term vapor pressure stability. The reduced pressure TGA method is effective for examining this stability. It was also determined (Fig. 9) that $Ba(hfa)_2 \cdot tet$ and $Ba(hfa)_2 \cdot mep$ have much improved vapor pressure temporal stability over $Ba(dpm)_2$, which decomposes substantially over the course of several hours in what is roughly an exponential decay in volatility. In contrast, $Ba(hfa)_2 \cdot tet$ and $Ba(hfa)_2 \cdot mep$ volatilities are stable within the resolution of the measurement over the course of 85 h. In practical use, we find that these precursors are stable over several months of MOCVD growth experiments and can be used essentially to depletion. Thus, the fluorinated alkaline earth precursors with polyether ancillary ligands are a significant step forward in the MOCVD of HTS materials.

In summary, reduced pressure TGA is a powerful tool for measuring the transport characteristics of metal-organic precursors under HTS film growth conditions. This is a valuable means to characterize newly developed precursors and to determine conditions for optimum film growth. At typical MOCVD pressures, diffusion effects are substantial and reactor design must account for this. Fluorinated barium β-diketonate polyether complexes are demonstrably more volatile and stable for film growth with the added advantage of being liquid under film growth conditions. The stable vapor pressure combined with the constant liquid surface ensures a far more reproducible MOCVD process.

B. MOCVD film growth and deposition mechanism

The MOCVD process is complex and can be roughly described by the following five steps: (i) volatilization of the precursor into the carrier stream; (ii) transport of the precursor to the hot reaction zone; (iii) chemisorption of the precursor and other reactive species, with subsequent surface migration, and decomposition; (iv) surface migration of metal ions with formation of the crystalline solid film; and (v) elimination of the organic by-products. In some MOCVD processes, the second step has been shown to be rate-limiting,[62,73–75] and reactor design considerations must provide a constant supply of gaseous precursor to the deposition zone area. As described in Sec. II, the present MOCVD reactor design, utilizing a laminar flow chamber with high aspect ratio, is employed to provide a uniform supply of precursor over a large substrate area. This design feature combined with precursors having stable vapor pressures facilitates the study of deposition kinetics.

To determine whether BaCaCuO(F) film growth kinetics are indeed limited by precursor mass transport, the relationship of precursor partial pressure to deposition rate must be analyzed. Figure 10 shows that as the carrier flow through the $Ba(hfa)_2 \cdot mep$ reservoir is increased from 0 to 150 sccm (with constant total carrier flow over the reaction zone), the BaF_2 deposition rate increases approximately to the 0.7 power of the precursor carrier gas flow, as expected for mass transport of a turbulent stream of subliming solid. Even though the carrier stream is not saturated with precursor, the mole-transport rate of the

precursor is easily controlled by precursor temperature and carrier flow. The concentration of precursor in the reactant stream is simply described by Eq. (5). The inset of Fig. 10 shows that the film deposition rate is indeed directly proportional to precursor mass transport rate and thus directly proportional to precursor concentration. This observation is consistent with a mass transport-limited film growth mechanism. Table III also shows that the gas phase stoichiometry is, within experimental error, identical to that of the deposited film as required for mass transport-limited deposition.

By general definition, mass transport-limited kinetics occur when the deposition rate is controlled by the transport of precursors to the reaction zone, or equivalently, is not limited by the kinetics of decomposition for the chemisorbed species. At lower substrate temperatures, film growth processes can be in the kinetic regime where the reaction rate is limited by the decomposition reaction, and thus a strong dependence of deposition rate on substrate temperature (typically increasing exponentially with temperature) is seen.[74] At higher temperatures (mass transport-limited kinetics) there is a weak dependence of deposition rate on temperature.

From the study of precursor transport and deposition rate as a function of substrate temperature, we conclude that the MOCVD growth process for BaCaCuO(F) films is mass transport-limited from 350–650 °C. Particularly, with $Ba(hfa)_2 \cdot mep$, $Ca(hfa)_2 \cdot tet$ $Cu(dpm)_2$, and an O_2/H_2O oxidizer stream, the onset of mass transport-limited kinetics begins near 350 °C [Fig. 12(a)]. This result is interesting because for $YBa_2Cu_3O_7$ MOCVD using *nonfluorinated* $Y(dpm)_3$, $Ba(dpm)_2$, and $Cu(dpm)_2$ precursors, the onset of a mass transport-limited regime is reported at temperatures greater than ~600 °C.[62] The decomposition of the present hfa coordinated ligands is apparently more facile, which is surprising since fluorinated ligands produce more Lewis acidic metal centers, which in turn form more stable adducts with polyethers. Since the film growth rates here are similar to those observed in other MOCVD studies with nonfluorinated precursors (~20 nm/min),[62] the depression in the onset temperature for mass transport-limited kinetics is not due to a lower mass transport rate. The present, large amount of H_2O in the oxidizer stream [conditions for Fig. 12(a)] could conceivably facilitate precursor decomposition by acting as a proton source to form volatile Hhfa by-products.[77–79] However, only a slight influence of H_2O on the onset temperature for mass-transport limited BaCaCuO(F) film growth is observed [Fig. 12(b)] and is surprising in view of the pronounced effect H_2O has in accelerating the decomposition of $Cu(hfa)_2$ during Cu° thin film growth.[77,79] Interestingly, at 400 °C, there is essentially no copper deposition. A possible explanation is that the decomposition products of $Ba(hfa)_2 \cdot mep$ and $Ca(hfa)_2 \cdot tet$ form $Cu(hfa)_2$ which then transports Cu from the film as in Eq. (4). There is precedent for $Cu(hfa)_2$ formation in the selective etching of Cu from Pd/Cu surfaces[99] as well as from CuO.[77,80] The temperature versus deposition rate plot for $Cu(dpm)_2$ alone in Fig. 12(c) shows a rather constant growth profile with the film growth rate gradually increasing with temperature. This is consistent with the results of Schmaderer *et al.*[62] which reveal a modest increase in CuO deposition rate from 400–900 °C with nonfluorinated precursors in similar kinetic studies. The diminution of CuO deposition at 400 °C seen in Fig. 12(b) requires the presence of fluorinated precursors and the absence of H_2O.

Mass spectral analysis of trapped by-products of the MOCVD deposition support a ligand exchange/etching mechanism, revealing the formation of $Cu(hfa)_2$ and Cu(hfa)(dpm). Although $Cu(hfa)_2$ is observed by mass spectral analysis with H_2O in the oxidizer stream, the effect on stoichiometry is minimal since gas phase and film metal stoichiometries are nearly identical (Table II). Large excesses of H_2O appear to retard the $Cu(hfa)_2$ formation under these conditions and to reduce copper etching, resulting in a film stoichiometry being identical to gas phase composition. This is consistent with findings that H_2O aids in the decomposition of $Cu(hfa)_2$ at temperatures as low as 250 °C.[77,79]

From the study of deposition rate as a function of precursor transport and substrate temperature, it can be concluded that the primary mechanism of BaCaCuO(F) MOCVD growth is mass transport-limited with the present precursor and reactor system. H_2O in the oxidizer stream has little effect on the onset of mass transport-limited film growth for BaO and CaO deposition; however, it does significantly affect CuO deposition. A ligand exchange mechanism is supported, therefore, by the observation of $Cu(hfa)_2$ as a by-product. With H_2O in the reactant stream, $Cu(hfa)_2$ formation is effectively eliminated, allowing mass transport limited deposition over a large temperature range (350–700 °C) for all three metals, resulting in a well-controlled MOCVD process.

C. BaCaCuO(F) precursor film deposition

Although the present MOCVD process is chemically complex, thin films of uniform composition over large areas can be readily grown. The conditions for the growth of BaCaCuO(F) films with 2 : 1 : 2 : Ba : Ca : Cu cation stoichiometry are given in Table I. The simple, modular reactor design affords a uniform deposition rate of 20 nm/min (±5% variation in measured thickness over a 16 cm^2 area). Due to the use of fluorinated metal-organic precursors, fluorides are readily incorporated in the film. Thus, to reduce the fluoride content, H_2O is used in the oxidizer stream to remove fluorides [presumably

as in Eq. (7)], as well as to stabilize the CuO deposition rate as previously mentioned. Furthermore, thin window EDX data for BaCaCuO(F) films grown between 733 and 780 °C with H_2O in the oxidizer gas stream show that fluorides are readily removed at temperatures approaching 780 °C. The films deposited at higher temperatures have high crystal growth rates, resulting in rough morphological features, and evidencing significant segregation of elements. Also, at higher temperatures, thermal buoyancy effects reduce the effective area of uniform deposition to $\sim 2 \times 4$ cm^2. At lower growth temperatures, higher nucleation rates are seen, and film morphology is markedly smoother. The stoichiometry of the various grains is then identical within SEM/EDX resolution. As described in the previous section, the fluoride content in the BaCaCuO(F) precursor films is not a critical factor, since it is removed in the subsequent thallination step. Thus, BaCaCuO(F) deposition can be carried out at relatively low temperatures (500 °C) to produce smooth film morphologies and to grow uniformly over large areas.

D. Tl-2212 phase formation and film characterization

Due to the high vapor pressure of Tl_2O over Tl-2212 at temperatures of phase formation (near 8 Torr)[100], *in situ* film growth is difficult, with only a few examples of successful growth of the low-thallium Tl-1212 and Tl-1223 phases.[101,102] An *in situ* route to high-T_c Tl-2212 remains elusive, and all high-quality films produced to date have been grown in a two-step process in which thallination of a (Tl)BaCaCuO precursor film is achieved by vapor diffusion as in Eq. (10). Typically a bulk pellet of superconductor is utilized to provide an equilibrium vapor pressure of Tl_2O for a given growth temperature and oxygen pressure.[103]

$$Ba_2Ca_{n-1}Cu_nO_{x(\mathrm{film})} + Tl_2O_{(g)} + O_2 \rightleftharpoons Tl_2Ba_2Ca_{n-1}Cu_nO_{4+2n(\mathrm{film})}\,. \quad (10)$$

To form the Tl-2212 phase, the present BCCO(F) precursor films are annealed over a 2:2:1:2 Tl_2O_3:BaO:CaO:CuO pellet at various O_2 pressures (the balance is Ar) at temperatures between 720 and 895 °C. The Tl-2212 phase is produced at annealing temperatures of 875, 820, and 720 °C in atmospheres of 100, 10, and 0% O_2, respectively. For annealing in 100% O_2, the temperature window for formation of phase-pure Tl-2212 is ±20 °C, with the Tl-1212 phase observed outside of this region. There are other examples of using reduced annealing temperatures with lower $P(O_2)$ to form the Tl-2212 phase.[104–107] Success from such methods is primarily due to the equilibrium in Eq. (10) wherein lower O_2 pressures drive the equilibrium to the left to produce more volatile Tl_2O. The two-zone furnace experiments of Aselage *et al.*, in which Tl_2O vapor pressure is controlled, support the conjecture that Tl_2O pressure control is the key to TBCCO phase stability.[100] The heating rate profile during the thallination anneal is also important in obtaining optimum film quality. At slow temperature ramps (2 °C/min), absorbed H_2O is driven off the Tl_2O source pellet (presumably from BaO + CaO) without forming volatile TlOH. With this Tl_2O_3 loss channel diminished, a more stable Tl_2O source is provided, and longer annealing times are possible without forming the undesired Tl-1212 phase. The resulting Tl-2212 films appear highly reflective, and the surface morphology is dominated by evidence of a melt during phase formation[104,108–110] [Fig. 16(a)]. As annealing temperatures are reduced, surface morphology becomes smoother, as has been qualitatively observed by other researchers.[108,111,112] At annealing temperatures below 860 °C in O_2, a notable increase in smoothness to under 100 nm is seen. XRD shows the epitaxial nature of film growth as demonstrated by c-axis orientation and in-plane alignment as determined by ϕ scans. The cross-sectional transmission electron microscopy [Fig. 18(c)] highlights the sharp interface between the superconductor and $LaAlO_3$ substrate, proving epitaxial growth.

The transport measurements provide further confirmation of the quality of the present MOCVD-derived films. Resistivity versus temperature behavior, shown in Fig. 19(a), exhibits the linear temperature dependence typical of pure HTS cuprates, with the low extrapolated residual resistivity and the resistivity magnitude approaching single crystal values. Other single-phase, PVD-derived Tl-2212 films exhibit similar T_c's of 95–105 K and similar normal state resistivity behavior. The lowest T_c MOCVD sample, which was processed in a pure O_2 atmosphere, showed evidence of oxygen overdoping, which would suppress the T_c value. The inductive measurements of the superconducting transitions for these films yield T_c values that agree very well with the resistively determined T_c values. This correlation indicates that the T_c is uniform throughout the entire film. Figure 19(b) illustrates an inductive T_c measurement, with $T_c = 103$ K and a transition width of 1.5 K. The transition widths obtained from the inductive measurements on other MOCVD-derived films ranged from 1–5 K. A narrow transition also indicates a uniform T_c in the sample. In terms of the measured critical current densities, the present J_c values determined by the transport and magnetic methods agree fairly well; e.g., J_c (77 K) $= 1.2 \times 10^5$ A/cm^2 by transport versus $J_c = 6.3 \times 10^5$ A/cm^2 from magnetization calculations. The transport J_c values are consistently somewhat lower, though, which

suggests that the J_c values are still limited by coupling between grains. The present MOCVD film values compare favorably with the best PVD-derived films, which have $T_c = 105$ K and J_c (80 K) $= 3 \times 10^6$ A/cm^2.[113] The microwave surface resistance measured for two MOCVD-derived Tl-2212 films is R_s (5 K) $=$ 0.40 mΩ at 10 GHz, which is comparable to the values achieved for PDV-derived films.[24] These results confirm that MOCVD growth processes can produce Tl-2212 thin films with the electrical properties acceptable for applications.

V. CONCLUSIONS

The successful MOCVD growth of Tl-2212 films as well as those of other HTS and non-HTS oxide materials relies critically on the availability of volatile precursors with stable vapor pressures. The reduced pressure TGA method described here allows the characterization of stable and volatile precursors such as Ba(hfa)$_2$ • mep, Ca(hfa)$_2$ • tet, and Cu(dpm)$_2$ in terms of precursor vapor pressure and diffusion effects. This method can be used as a powerful tool to assess the volatility of newly developed MOCVD precursors and to expeditiously target optimum film growth conditions. All of these precursors are suitably volatile for HTS MOCVD, and of particular importance is that liquid Ba(hfa)$_2$ • mep at 116 °C has the same volatility as Ba(dpm)$_2$ at a temperature where decomposition of the latter is substantial (200 °C in a total pressure of 5 Torr N_2). An efficient reactor design permits uniform deposition of BaCaCuO(F) films over a 5×5 cm^2 area and allows elucidation of the deposition kinetics for these hfa-based precursors. The BaCaCuO(F) film deposition process is mass transport-limited, with the onset of mass transport-limited growth at a remarkably low temperature of 350 °C for a growth rate of 20 nm/min. H_2O in the oxidizer stream has little effect on the onset of mass-transport limited film growth rates for Ba and Ca deposition; however, it markedly affects CuO deposition. An interesting precursor ligand exchange process is evidence by the detection of Cu(hfa)$_2$ in the by-products, correlating with regimes of reduced CuO deposition. With H_2O in the reactant stream, the CuO etching reaction is effectively eliminated, resulting in mass transport-limited deposition over the large temperature range of 350–700 °C for all precursors. Thus, these fluorinated alkaline earth precursors can be implemented in a well-controlled MOCVD process.

The MOCVD-derived BaCaCuO(F) films are readily annealed in the presence of Tl_2O to form high quality Tl-2212 films in an efficient, open-flow process. It is found that annealing temperatures can be reduced at lower O_2 pressures. At 1.0 atm O_2 pressure, the reduced annealing temperature brings about a substantial reduction in surface roughness, with anneals below 860 °C giving an rms roughness ~80 nm. XRD and cross-sectional TEM data demonstrate the epitaxial nature of film growth and the crystalline quality.

Transport measurements further assay the properties of the MOCVD-derived Tl-2212 films. The variable temperature resistivity data indicate $T_c = 103$ K, while sharp transitions are also seen in inductive measurements. At 77 K $J_c = 1.2 \times 10^5$ A/cm^2. Importantly, $R_s = 0.40$ mΩ at 5 K, 10 GHz, approaching the lowest values reported for PVD-derived films. Thus, this well-controlled MOCVD processing based on fluorinated β-diketonate/polyether ligands yields Tl-2212 thin films suitable for microwave device applications.

ACKNOWLEDGMENTS

This research was supported by the National Science Foundation through the Science and Technology Center for Superconductivity (Grant No. DMR 91-20000), by the Northwestern Materials Research Center (Grant No. DMR 9632472), and by NSF/ONR/ARPA (CHE-9421910/N00014-95-1-0717). We thank Dr. Ronald Nordin of AT&T Laboratories (Naperville, IL) for assistance with microwave measurements.

REFERENCES

1. R. C. Black, F. C. Wellstood, E. Dantsker, A. H. Miklich, D. Koelle, F. Ludwig, and J. Clarke, IEEE Trans. Appl. Supercond. **5**, 2137–2141 (1995).
2. L. P. Lee, K. Char, M. S. Colclough, and G. Zaharchuk, Appl. Phys. Lett. **59**, 3051–3053 (1991).
3. R. H. Koch, J. Z. Sun, V. Foglietta, and W. J. Gallagher, Appl. Phys. Lett. **67**, 709–711 (1995).
4. J. E. Nordman, Supercond. Sci. Technol. **8**, 681–699 (1995).
5. J. S. Satchell, R. G. Humphreys, J. A. Edwards, and N. G. Chew, IEEE Trans. Appl. Supercond. **3**, 2273–2276 (1993).
6. M. J. Burns, K. Char, B. F. Cole, W. S. Ruby, and S. A. Sachtjen, J. Appl. Phys. **75**, 1435–1437 (1992).
7. F. C. Wellstood, J. J. Kingston, and J. Clarke, J. Appl. Phys. **75**, 683–702 (1994).
8. For recent progress, see *High-Temperature Superconducting Detectors: Bolometric and Nonbolometric,* edited by M. Nahum and J-C. Villegier (SPIE Sympos. Proc. 2159, 1994), pp. 1–191.
9. D. Janik, D. May, H. Wolf, and R. Schneider, IEEE Trans. Appl. Supercond. **3**, 2148–2151 (1993).
10. For recent progress, see IEEE Trans. Appl. Supercond.; Vol. 5, edited by A. F. Clark,
11. For recent progress, see *High-T_c Microwave Superconductors and Applications,* edited by R. B. Hammond and R. S. Withers (SPIE Sympos. Proc. 2156, 1994), pp. 1–223.
12. N. Newman, Mater. Sci. Forum **130–132**, 553–578 (1993).
13. K. Suzuki, S. Fujino, T. Takenaka, K. Yamaguchi, T. Morishita, K. Imai, F. Suginoshita, N. Yazawa, and M. Kobayashi, Appl. Supercond. **1**, 1575–1593 (1993).
14. R. Weigel, A. A. Valenzuela, and P. Russer, Appl. Supercond. **1**, 1595–1604 (1993).

15. G-C. Liang, D. Zhang, C-F. Shih, M. E. Johansson, R. S. Withers, A. C. Anderson, and D. E. Oates, IEEE Trans. Appl. Supercond. **5**, 2652–2655 (1995).
16. D. C. DeGroot, J. A. Beall, R. B. Marks, and D. A. Rudman, IEEE Trans. Appl. Supercond. **5**, 2272–2275 (1995).
17. W. Rauch, E. Gornik, G. Solkner, A. A. Valenzuela, H. Behner, and G. Gieres, Appl. Supercond. **2**, 417–423 (1994).
18. D. Jing, K. Shao, C. H. Cao, L. X. Zhang, G. Jiao, Z. J. Zhang, S. Q. Li, C. N. Guo, B. C. Yang, X. P. Wang, G. C. Xiong, and Q. J. Lian, Supercond. Sci. Technol. **7**, 792–794 (1994).
19. J. Kruse, W. H. Chang, D. Scherrer, M. Feng, M. Scharen, A. Cardona, and R. Forse, Appl. Phys. Lett. **65**, 2478–2480 (1994).
20. Z. Wu, Supercond. Sci. Technol. **8**, 464–469 (1995).
21. S. A. Maas, IEEE Trans. Microwave Theory Technol. **39**, 1445–1675 (1991).
22. Z. Z. Sheng and A. M. Hermann, Nature (London) **332**, 138–139 (1988).
23. W. L. Holstein, L. A. Parisi, C. Wilker, and R. B. Flippen, IEEE Trans. Appl. Superconductivity **3**, 1197–1200 (1993).
24. W. L. Holstein, L. A. Parisi, C. Wilker, and R. B. Flippen, Appl. Phys. Lett. **60**, 2014–2016 (1992).
25. R. B. Hammond, G. V. Negrete, L. C. Bourne, D. D. Strother, A. H. Cardona, and M. M. Eddy, Appl. Phys. Lett. **57**, 825–827 (1990).
26. M. M. Eddy, J. Z. Sun, R. D. Hammond, L. Drabeck, I. B. Ferreira, K. Holczer, and G. Grüner, J. Appl. Phys. **70**, 496–498 (1991).
27. L. D. Chang, M. J. Moskowitz, R. B. Hammond, M. M. Eddy, W. L. Olson, D. D. Casavant, E. J. Smith, M. Robinson, L. Drabeck, and G. Grüner, Appl. Phys. Lett. **55**, 1357–1359 (1989).
28. G. Subramanyam, V. J. Kapoor, C. M. Chorey, and K. B. Bhasin, Appl. Supercond. **1**, 1605–1614 (1993).
29. S. Huber, M. Manzel, H. Bruchlos, S. Hensen, and G. Müller, Physica C **244**, 337–340 (1995).
30. G. Subramanyam, V. J. Kapoor, C. M. Chorey, and K. B. Bhasin, J. Appl. Phys. **72**, 2396–2403 (1992).
31. S. L. Yan, L. Fang, M. S. Si, H. L. Cao, Q. X. Song, J. Yan, X-D. Zhou, and J. M. Hao, Supercond. Sci. Technol. **7**, 681–684 (1991).
32. N. Hamaguchi, R. Boestler, R. Gardiner, and P. Kirlin, Physica C **185–189**, 2023–2024 (1991).
33. B. J. Hinds, J. L. Schindler, B. Han, D. A. Neumayer, D. C. DeGroot, T. J. Marks, and C. R. Kannewurf, in *Metal-Organic Chemical Vapor Deposition of Electronic Ceramics,* edited by S. B. Desu, D. B. Beach, B. W. Wessels, and S. Gokoglu (Mater. Res. Soc. Symp. Proc. **335**, Pittsburgh, PA, 1994), pp. 273–278.
34. G. V. Negrete and R. B. Hammond, SPIE **1477**, 36–44 (1991).
35. S. C. Wu, C. Y. Yeh, F. H. Chen, T. Y. Tseng, C. Wang, H. L. Chang, and H. J. Wang, Appl. Phys. Lett. **65**, 3281–3283 (1994).
36. A. M. Hermann, R. M. Yandrofski, J. F. Scott, A. Naziripour, D. Galt, J. C. Price, J. Cuchario, and R. K. Ahrenkiel, J. Supercond. **7**, 463–469 (1994).
37. D. L. Schulz and T. J. Marks, Adv. Mater. **6**, 719–730 (1994).
38. D. L. Schulz and T. J. Marks, in *CVD of Nonmetals,* edited by W. Rees (VCH Publishers, in press).
39. M. Leskelä, H. Mösla, and L. Niinistö, Supercond. Sci. Technol. **6**, 627–656 (1993).
40. K. H. Dahmen and T. Gerfin, Prog. in Cryst. Growth and Charact. of Mater. **27**, 117–161 (1993).
41. J. Hu, D. J. Miller, D. L. Schulz, B. Han, D. A. Neumayer, B. J. Hinds, and T. J. Marks, Physica C **210**, 97–105 (1993).
42. N. Hamaguchi, R. Gardiner, and P. S. Kirlin, Appl. Surf. Sci. **48/49**, 441–445 (1991).
43. J. A. Ladd, B. T. Collins, J. R. Matey, J. Zhao, and P. Norris, Appl. Phys. Lett. **59**, 1368–1370 (1991).
44. D. L. Schulz, D. S. Richeson, G. Malandrino, D. Neumayer, T. J. Marks, D. C. DeGroot, J. L. Schindler, T. Hogan, and C. R. Kannewurf, Thin Solid Films **216**, 45–48 (1992).
45. G. Malandrino, D. S. Richeson, T. J. Marks, D. C. DeGroot, J. L. Schindler, and C. R. Kannewurf, Appl. Phys. Lett. **58**, 182–184 (1991).
46. B. J. Hinds, D. L. Schulz, D. A. Neumayer, B. Han, T. J. Marks, Y. Y. Wang, V. P. Dravid, J. L. Schindler, T. P. Hogan, and C. R. Kannewurf, Appl. Phys. Lett. **65**, 231–233 (1994).
47. S. Koike, T. Nabatame, and I. Hirabayashi, Jpn. J. Appl. Phys. Lett. **32**, L828–L831 (1993).
48. D. S. Richeson, L. M. Tonge, X. K. Wang, H. O. Marcy, T. J. Marks, J. B. Ketterson, R. P. H. Chang, and C. R. Kannewurf, Appl. Phys. Lett. **55**, 2778–2780 (1989).
49. H. J. Scheel, M. Berkowski, and B. Chabot, J. Cryst. Growth **115**, 19–30 (1991).
50. M. L. Hitchman, S. H. Shamlian, D. D. Gilliland, D. J. Cole-Hamilton, S. C. Thompson, S. L. Cook, and B. C. Richards, in *Metal-Organic Chemical Vapor Deposition of Electronic Ceramics,* edited by S. B. Desu, D. B. Beach, B. W. Wessels, and S. Gokoglu (Mater. Res. Soc. Symp. Proc. **335**, Pittsburgh, PA, 1994), pp. 249–260.
51. I. M. Watson, M. P. Atwood, and S. Haq, Supercond. Sci. Technol. **7**, 672–680 (1994).
52. K. S. Chou and G. J. Tsai, Thermochimica Acta **240**, 129–139 (1994).
53. P. Tobaly and G. Lanchec, J. Chem. Thermodyn. **25**, 503–510 (1993).
54. R. Sato, K. Tkahashi, M. Yoshino, H. Kato, and S. Ohshima, Jpn. J. Appl. Phys. **32**, 1590–1594 (1993).
55. T. Hashimoto, H. Koinuma, M. Nakabayashi, T. Shiraishi, Y. Suemune, and T. Yamamoto, J. Mater. Res. **7**, 1336–1340 (1992).
56. S. C. Thompson, D. J. Cole-Hamilton, D. D. Gilliland, M. L. Hitchman, and J. C. Barnes, Adv. Mater. Opt. Electron. **1**, 81–97 (1992).
57. S. B. Turnipseed, R. M. Barkley, and R. E. Seivers, Inorg. Chem. **30**, 1164 (1991).
58. H. Busch, A Fink, A Müller, and K. Samwer, Supercond. Sci. Technol. **6**, 42–45 (1993).
59. S. R. Drake, M. B. Hursthouse, K. M. A. Malik, and D. J. Otway, J. Chem. Soc. Dalton Trans., 2883–2890 (1993).
60. K. Timmer, C. I. M. A. Spee, A. Mackor, H. A. Meinema, A. L. Spek, and P. v. d. Sluis, Inorg. Chim. Acta **190**, 109–117 (1991).
61. R. Gardiner, D. W. Brown, P. S. Kirlin, and A. L. Rheingold, Chem. Mater. **3**, 1053–1059 (1991).
62. F. Schmaderer, R. Hubre, H. Oetzmann, and G. Wahl, in *11th Int. Conf. of CVD,* edited by K. E. Spear and G. W. Cullen (ECS, Pennington, NJ, 1990), pp. 211–218.
63. F. Schmaderer, R. Huber, H. Oetzmann, and G. Wahl, Appl. Surf. Sci. **46**, 53–60 (1990).
64. D. A. Neumayer, D. B. Studebaker, B. J. Hinds, C. L. Stern, and T. J. Marks, Chem. Mater. **6**, 878–880 (1994).
65. D. L. Schulz, D. A. Neumayer, and T. J. Marks, Inorg. Synth. **31**, 1 (1997).
66. G. Rossetto, A. Polo, F. Benetollo, M. Porchia, and P. Zanella, Polyhedron **11**, 979–985 (1992).
67. H. Moffat and K. F. Jenson, J. Cryst. Growth **77**, 108 (1986).
68. L. W. Lyding, H. O. Marcy, T. J. Marks, and C. R. Kannewurf, IEEE Trans. Instrum. Meas. **37**, 76–80 (1988).
69. J. L. Schindler, Ph.D. Thesis, Northwestern University (1995).

70. R. C. Taber, Rev. Sci. Instrum. **61**, 2200–2206 (1990).
71. D. C. Degroot, T. P. Hogan, C. R. Kannewurf, D. B. Buchholz, R. P. H. Chang, F. Gao, M. Feng, and R. A. Nordin, Physica C **222**, 271–277 (1994).
72. A. H. P. Skelland, *Diffusional Mass Transfer* (John Wiley & Sons, New York, 1974), pp. 221–225.
73. K. F. Jensen, in *Chemical Vapor Deposition: Principle and Application,* edited by M. L. Hitchman and K. F. Jensen (Academic Press, London, 1993), pp. 31–90.
74. G. B. Stringfellow, *Organometallic Vapor-Phase Epitaxy* (Academic Press Inc., New York, 1989), pp. 265–284.
75. W. S. Kern and V. S. Ban, in *Thin Film Processes,* edited by J. L. Vossen and W. S. Kern (Academic Press, San Diego, 1978), pp. 257–331.
76. K. Zhang and A. Erbil, in *Materials Science Forum,* edited by J. J. Pouch, S. A. Alterovitz, R. R. Romanofsky, and A. F. Hepp, (Aedermannsdorf, Switzerland, 1993), Vols. 130–132, pp. 255–268.
77. J. Pinkas, J. C. Huffman, D. V. Baxter, M. H. Chrisholm, and K. G. Caulton, Chem. Mater. **7**, 1589–1596 (1995).
78. A. E. Kaloyeros, B. Zheng, I. Lou, J. Lau, and J. W. Hellgeth, Thin Solid Films **262**, 20–30 (1995).
79. B. Lecohier, J. B. Calpini, J-M. Philippoz, and H. v. d. Bergh, J. Appl. Phys. **72**, 2022–2026 (1992).
80. F. Rousseau, A. Jain, T. T. Kodas, M. J. Hampden-Smith, J. D. Farr, and R. J. Muenchausen, J. Mater. Chem. **2**, 893–894 (1992).
81. A. Jain, T. T. Kodas, and M. J. Hampden-Smith, Thin Solid Films **269**, 51–56 (1995).
82. T. Wang and P. C. Uden, J. Chromatography **517**, 185–192 (1990).
83. Joint Committee for Powder Diffraction Standards (JCPDS), Center for Diffraction Data, 1601 Park Lane, Swathmore, PA 19081, No. 4-452 (BaF2), No. 5-661 (CuO), No. 34-0282 ($CaCu_2O_3$).
84. D. Cubicciotti and H. Eding, J. Chem. Eng. Data **10**, 343–345 (1967).
85. F. Keneshea and D. Cubicciotti, J. Phys. Chem. **71**, 1958 (1967).
86. W. L. Holstein, in *Metal-Organic Chemical Vapor Deposition of Electronic Ceramics,* edited by S. B. Desu, D. B. Beach, B. W. Wessels, and S. Gokoglu (Mater. Res. Soc. Symp. Proc. **335**, Pittsburgh, PA, 1994), pp. 165–170.
87. C. P. Bean, Phys. Rev. Lett. **8**, 250 (1962).
88. D. C. DeGroot, T. P. Hogan, C. R. Kannewurf, D. B. Buchholz, R. P. H. Chang, F. Gao, M. Feng, and R. A. Nordin, Physica C **222**, 271–277 (1994).
89. F. DiMeo, Jr., B. W. Wessels, D. A. Neumayer, T. J. Marks, J. L. Schindler, and C. R. Kannewurf, in *Metal-Organic Chemical Vapor Deposition of Electronic Ceramics,* edited by S. B. Desu, D. B. Beach, B. W. Wessels, and S. Gokoglu (Mater. Res. Soc. Symp. Proc. **335**, Pittsburgh, PA, 1994), pp. 285–290.
90. B. C. Richards, S. L. Cook, D. L. Pinch, G. W. Andrews, G. Lengeling, B. Schulte, H. Jürgensen, Y. Q. Shen, P. Vase, T. Freltoft, C. I. M. A. Spee, J. L. Linden, M. L. Hitchman, S. H. Shamlian, and A. Brown, Physica C **252**, 229–236 (1995).
91. Y. Mizushima and I. Hirabayashi, Physica C **235–240**, 577–578 (1994).
92. S. H. Shamlian, M. L. Hitchman, S. L. Cook, and B. C. Richards, J. Mater. Chem. **4**, 81–85 (1994).
93. G. M. Rosenblatt, in *Treatise on Solid State Chemistry,* edited by N. B. Hannay (Plenum Press, New York, 1976), Vol. 6A, pp. 165–240.
94. I. Langmuir, Phys. Rev. **II**, 329 (1913).
95. J. Santiso and A. Figueras, J. Phys. IV **3**, 353–360 (1993).
96. Y. Takahashi, K. Matsuzaki, M. Iijima, E. Fukada, S. Tsukahara, Y. Murakami, and A. Maesono, Jpn. J. Appl. Phys. **32**, L875–L878 (1993).
97. N. E. Fedotova, I. K. Igumenov, V. I. Mamatyuk, and G. V. Sidorenko, J. Phys. IV **5**, 431–438 (1995).
98. N. B. Hannay, *Treatise on Solid State Chemistry Volume 6A Surfaces* (Plenum Press, New York, 1976).
99. W. Lin, T. H. Warren, R. G. Nuzo, and G. S. Girolami, J. Am. Chem. Soc. **115**, 11 644–11 645 (1993).
100. T. L. Aselage, E. L. Venturini, and S. B. v. Deusen, J. Appl. Phys. **75**, 1023–1031 (1994).
101. D. W. Face and J. P. Nestlerode, Appl. Phys. Lett. **61**, 1838–1840 (1992).
102. N. Takahashi, A. Koukitu, H. Seki, and Y. Kamioka, Jpn. J. Appl. Phys. Lett. **33**, L840–L842 (1994).
103. R. Sugise, M. Hirabayashi, N. Terada, M. Jo, F. Kawashima, and H. Ihara, Jpn. J. Appl. Phys. Lett. **27**, L2314–L2316 (1988).
104. W. Y. Lee, S. M. Garrison, M. Kawasaki, E. L. Venturini, B. T. Ahn, R. Boyers, J. Salem, R. Savoy, and J. Vazquez, Appl. Phys. Lett. **60**, 772–774 (1992).
105. S. L. Yan, L. Fang, M. S. Si, H. L. Cao, Q. X. Song, J. Yan, X. D. Zhou, and J. M. Hao, Supercond. Sci. Technol. **7**, 681–684 (1994).
106. S. L. Yan, L. Fang, Q. X. Song, J. Yan, Y. P. Zhu, J. H. Chen, and S. B. Zhang, Appl. Phys. Lett. **63**, 1845–1847 (1993).
107. K. S. Nanjundaswamy, A. Manthiram, and J. B. Goodenough, Physica C **207**, 339–346 (1993).
108. D. S. Ginley, J. F. Kwak, E. L. Venturini, B. Morosin, and R. J. Baughman, Physica C **160**, 42–48 (1989).
109. C. T. Cheung and E. Ruckenstein, J. Mater. Res. **5**, 245–250 (1990).
110. P. E. D. Morgan, R. M. Housely, J. R. Porter, and J. J. Ratto, Physica C **176**, 279–284 (1992).
111. T. Nabatame, Y. Saito, K. Aihara, T. Kamo, and S-P. Matsuda, Jpn. J. Appl. Phys. **29**, L1813–L1815 (1990).
112. J. Chrzanowski, X. M. Burany, A. E. Curzon, J. C. Irwin, B. Heinrich, N. Fortier, and A. Cragg, Physica C **207**, 25–36 (1993).
113. W. L. Holstein, C. Wilder, D. B. Laubacher, D. W. Face, P. Pang, M. S. Warrington, C. F. Carter, and L. A. Parisi, J. Appl. Phys. **74**, 1426–1430 (1993).